J. Fluid Mech. (2005), *vol.* 537, *pp.* 349–385.
doi:10.1017/S0022112005005148 Printed in the United Kingdom

Investigation of noise sources in high-speed jets via correlation measurements

By J. PANDA[1,2], R. G. SEASHOLTZ[2] AND K. A. ELAM[2,3]

[1]Ohio Aerospace Institute, Brook Park, OH
[2]NASA Glenn Research Center, Cleveland, OH
[3]Akima Corporation, Fairview Park, OH

(Received 22 March 2003 and in revised form 22 February 2005)

To locate noise sources in high-speed jets, the far-field sound pressure fluctuations p' were correlated with each of density ρ, axial velocity u, radial velocity v, ρuu and ρvv fluctuations measured from various points in jet plumes. Detailed surveys were conducted in fully expanded, unheated plumes of Mach 0.95, 1.4 and 1.8. The velocity and density fluctuations were measured simultaneously using a recently developed non-intrusive point measurement technique based on molecular Rayleigh scattering. The technique uses a continuous-wave narrow line-width laser, Fabry–Perot interferometer and photon counting electronics. Laser light scattered by air molecules from a 1.06 mm long region on the narrow beam was collected and spectrally resolved by the interferometer. It was observed that the fluctuation spectra for air density inside the plume were in general similar to those of axial velocity spectra, while the radial velocity spectra were somewhat different. For the correlation study, microphone polar angles were varied from 30° to 90° to the jet axis. The sound pressure fluctuations p' at the shallowest 30° angle provided the highest correlation with turbulent fluctuations. The correlations sharply decreased as the polar angle was increased to 60°, beyond which all data mostly fell below the experimental noise floor. Among all turbulent fluctuations $\langle \rho uu; p' \rangle$ correlations showed the highest values. Correlation with the first-order terms $\langle \rho' \bar{u}\bar{u}; p' \rangle$, $\langle \bar{\rho}\bar{u}u'; p' \rangle$ and third-order terms $\langle \rho' u'u'; p' \rangle$ was higher than that from the second-order terms $\langle \bar{\rho}u'u'; p' \rangle$ and $\langle \bar{u}\rho'u'; p' \rangle$. Both $\langle v'; p' \rangle$ and $\langle \rho vv; p' \rangle$ correlations with the 90° microphone signal fell below the experimental noise floor, while that from the shallow 30° microphone showed weaker values. By moving the laser probe to various locations in the jet, it was found that the strongest noise source lay downstream of the end of the potential core and extended many diameters beyond. Correlation measurements from turbulent fluctuations along the lip shear layer showed a Mach-number dependency: significant values were measured in supersonic jets, while correlations fell below the noise floor for subsonic jets. Various additional analyses showed that fluctuations from large coherent structures mostly contributed to the measured correlation, while that from small-scale structures fell below the noise floor.

1. Introduction

The last six decades have not produced a unanimously accepted answer to the simple question of what produces noise from a jet flow. A vast number of earlier and current workers have relied upon the acoustic analogy framework of Lighthill (1954), Lilley (1974) and others. In the last few years there has been some opposition to such

an answer, based on multiple issues (Fedorchenko 2000; Tam 2001). Besides the U^8 dependence of sound intensity, which only confirms proper dimensional scaling, there is a lack of experimental verification of Lighthill sources. This lack of verification has fuelled the controversy. Experimentally, thus far it has been impossible to directly measure the stress tensors. Even if we can measure all possible turbulence statistics, the next step to determine which parts of the turbulent fluctuations actually radiate in the far field becomes more difficult. Since the problem of noise source identification is ultimately tied to knowledge of turbulent fluctuations, there have been significant theoretical efforts to explain sources based on the structure of turbulence. With the realization that turbulence is not only small random eddies, but also long coherent fluctuations, came the instability-wave-based sound-generation theories of Morris & Tam (1979) and Tam & Burton (1984). Michalke (1977, 1983) decomposed turbulent fluctuations in circular jets into azimuthal modes with axial and radial coherent length scales. Each azimuthal mode would be related to a corresponding instability wave. Michalke's analysis showed that only the modes with low azimuthal order (axisymmetric or first helical) can significantly contribute to the far-field noise. On the other hand, the small-scale turbulence is a very inefficient radiator. Nevertheless, the radiation inefficiency is compensated for by the large population of such small eddies present in any turbulent shear flows. Tam, Golebiowski & Seiner (1996) proposed that there are two components of jet mixing noise, one from the large turbulence structures and the other from the fine-scale turbulence of the jet flow. The noise from the large turbulence structures dominates the downstream direction. For high subsonic jets this extends from 0° (exhaust angle) to approximately 60°. Beyond 60° the noise is mainly from the fine-scale turbulence. Empirical similarity spectra, derived using this idea, are found to provide a good match to the jet noise data (Tam & Zaman 2000).

Experimentally, the task of jet noise source identification takes simpler routes. The common practice of using microphone arrays, elliptical and spherical mirrors in the far field to determine source location have both advantages and drawbacks. One advantage lies in the simplicity and the avoidance of measuring the complex turbulent flow, which is modelled simply as a distribution of monopoles. However, the noise sources are not monopoles, and the sound waves undergo a large amount of scattering before arriving at the far field; a linear extrapolation of the sound path may lead to a dubious conclusion. There is a need to determine noise sources by independent means, which is the motivation for the present work. It can be argued that such an independent means can neither be achieved by only turbulence measurement/simulation, nor by sole observations from the far field, but through a simultaneous measurement of cause (turbulent fluctuations) and effect (far-field noise).

The direct correlation between the cause and effect was originally proposed by Siddon (see Rackl 1973; Siddon 1973) to locate sound sources, and during the 1970s many experimentalists had adopted the method. Usually, velocity (Lee & Ribner 1972; Seiner & Reethof 1974; Schaffar 1979; Richarz 1980, and others) or pressure fluctuations (Hurdle, Meecham & Hodder 1974; Armstrong, Michalke & Fuchs 1977, and others) in the jet were correlated with the sound pressure fluctuations measured by a fixed microphone. An attractive feature of this method is that the effects of scattering, absorption and refraction on sound radiation are automatically included by virtue of simultaneously extracting information from both the flow and acoustic fields. The present work is based upon the causality idea proposed in these earlier works. One of the disadvantages of the earlier works, the lack of a non-intrusive turbulence measurement tool, however, is eliminated by the use of a

molecular Rayleigh-scattering technique. The noise produced by intrusive hot-wire probes (Seiner 1974, and others) or microphones (Hurdle *et al.* 1974, and others) placed inside the flow, contaminated much of the earlier data. Use of laser-Doppler velocimetry (LDV) by Schaffar (1979) and Richarz (1980), among others, somewhat avoided the issue of probe-intrusiveness. Nevertheless, the important issue of accuracy in velocity spectra measurements using LDV has lingered. Another approximation, used by earlier workers in evaluating Lighthill's stress tensors, is that the contribution from the density fluctuations is negligible: $\rho U_i U_j \approx \bar{\rho} U_i U_j$, where $\bar{\rho}$ is time-averaged density. This might be reasonable for low-speed unheated flows, but is unreasonable for the high-speed jets of present interest. It is to be noted that the role of density in Lighthill's formulation is ambivalent; every term in the right- and left-hand sides of Lighthill's equation contains density dependence.

The molecular Rayleigh scattering based technique has been advanced to simultaneously measure density and velocity fluctuations spectra in high-speed flow for the first time by Seasholtz, Panda & Elam (2001, 2002). Fluctuations occurring over a frequency range of 0 to 50 kHz have been measured. The technique is based on laser light scattering from the gas molecules present in air. Since neither seed particles nor intrusive probes are used, the technique is free from various problems faced by previous workers. Implementation of the technique requires special attention to the cleanliness of the air stream, isolation of the sensitive optical components from jet noise, use of Fabry–Perot interferometer and low-level light measuring electronics. These aspects are discussed in the text.

An in-depth study of correlation between flow density fluctuations and sound pressure fluctuations, from the peak noise emission direction, has been reported by Panda & Seasholtz (2002). A field survey of density fluctuations presented in that paper (for the same operating conditions used in the present) showed that except for the progressive stretching of the potential core, the turbulent fluctuations were similar over the Mach number range, while the noise characteristics were grossly different. The present work is a continuation and banks on the additional capability of measuring one component of velocity fluctuations. The fluctuating stress terms ρuu and ρvv are measured and correlated with sound pressure fluctuations from various polar angles. Observations on the location of sound sources measured in the present work are consistent with the earlier data. It is also to be noted that the time-average profiles of the jets under study were presented in earlier publications. Radial and centreline surveys of time-average density, standard deviation and spectral features of density fluctuations can be found in Panda & Seasholtz (2002). Surveys of time-average velocity and temperature for the same jets, measured by the Rayleigh-scattering technique can be found in Panda *et al.* (2004).

1.1. *Fundamentals of flow measurement using the Rayleigh-scattering principle*

A simplified description of the measurement process, using laser-induced Rayleigh scattering is shown in figure 1. When a laser beam is allowed to pass through a gas, the molecules present in the gas cause inelastic and elastic light scattering. Raman scattering is an example of inelastic scattering, where the scattered light has significant frequency shift from the incident light. Rayleigh scattering is the elastic part, which does not suffer frequency change, except for the Doppler shift from the motion of the molecules. The Rayleigh-scattering process describes most ($\sim 99\,\%$) of the molecular scattered light. A good discussion of the fundamental principle of Rayleigh scattering can be found in Miles, Lempert & Forkey (2001) and the references therein. In the present experiment, scattered light is collected and spectrally resolved to measure

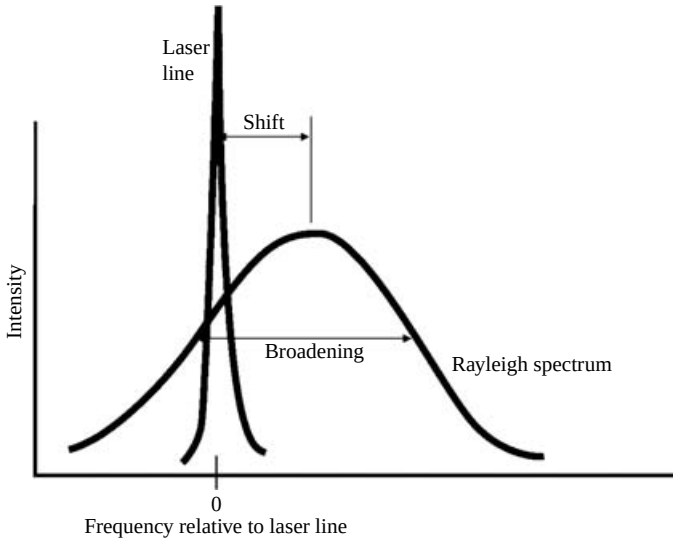

FIGURE 1. Schematic of Rayleigh spectrum for a dilute gas.

velocity. Since the Doppler-shift frequency is relatively small, a narrow linewidth incident laser beam is necessary to resolve the Rayleigh spectrum. Even if the gas medium is stationary, the random thermal motion of the gas molecules creates a wide range of Doppler shift – resulting in a spectral broadening of the collected light. The full width at half maximum (FWHM) is a function of the distribution of molecular velocities and, therefore, is a measure of gas temperature. In the case of a moving gas media, the bulk motion is superimposed on the random velocity of the individual molecules; therefore, separation between the peaks of the incident laser line and the Rayleigh spectrum provides a measure of the bulk velocity. This principle becomes clear from an examination of the optical spectrum of the Rayleigh scattered light $\Re(\nu - \nu_0)$ for a low-density gas moving with a bulk velocity $\boldsymbol{U}$:

$$\Re(\nu - \nu_0)\,\mathrm{d}f = \frac{2\sqrt{\pi}}{a_p k}\exp\left[-\left\{\frac{2\pi(\nu - \nu_0) - \boldsymbol{k}\cdot\boldsymbol{U}}{a_p k}\right\}^2\right]\mathrm{d}f \tag{1}$$

where, ν is scattered light frequency, ν_0 is the incident laser frequency, $\boldsymbol{k}$ is the scattering wavenumber, and a_p, the 'most probable molecular speed', is related to the local sound speed a and ratio of specific heat γ through $a_p = (2/\gamma)^{1/2}a$. The width of the spectrum depends on $a_p k$, which is proportional to the square root of the temperature; the peak of the spectrum is shifted by the Doppler shift $\boldsymbol{k}\cdot\boldsymbol{U}$; and the total light under the Rayleigh spectrum is proportional to the molecular number density and provides a measure of gas density. Thus, a single Rayleigh spectrum carries information of one component of gas bulk velocity, temperature and density.

This basic principle has been used in the past to measure *time-averaged* quantities (Elliott & Sammimy 1996; Forkey, Lempert & Miles 1998; Panda *et al.* 2004). Since density variation modulates the total scattered light, unsteady density fluctuations are easier to measure (Panda & Seasholtz 2002, among others). Extension of the Rayleigh-scattering technique to measure unsteady velocity fluctuation has remained a challenge. Seasholtz *et al.* (2002) have simultaneously measured the time variation of density and velocity fluctuations in free jets. Earlier efforts that contributed towards the present set-up can be found in Seasholtz *et al.* (2001) and Seasholtz & Panda

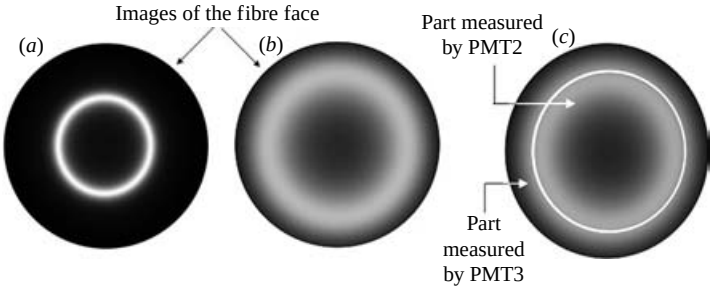

FIGURE 2. Fringes formed after passing through the Fabry–Perot interferometer by (*a*) incident laser light; (*b*) Rayleigh scattered light; (*c*) splitting of Rayleigh image to measure velocity fluctuations.

(1999, 2000). The present set-up is for a point-measuring system; a continuous wave laser was used, and scattered light from a small region on the beam was collected and analysed. The scattered light from the probe volume positioned at various points in the flow field was collected and transferred to a nearby location for spectral analysis via an optical fibre. The spectral analysis was performed using a Fabry–Perot interferometer.

To illustrate the unsteady velocity measurement process, first the nature of a fringe formed by the interferometer is shown in figure 2. The interferometer images the fibre-end delivering the scattered light. Since the fibre diameter is small, the field of view in the image covers a fraction of the free spectral range. The spectral analysis is a two-step process. First, a small portion of the light directly out of the laser beam is imaged through the interferometer (the Rayleigh scatterded light is blocked; instead a part of the unscattered incident laser beam is split and light is coupled to the fibre). The narrow line width of the laser makes a sharp narrow ring in this image (figure 2*a*). In the second step, the Rayleigh-scattered light from a moving gas medium is passed through the fibre. The image formed by the Fabry–Perot interferometer (figure 2*b*) is different: a diffused ring with a different ring diameter results. The radial shift in the peak intensity locations between the Rayleigh and the reference images is related to the Doppler shift associated with the bulk motion of the air stream (the diffused nature of the Rayleigh image is due to the thermal broadening). Since the laser frequency, and therefore, the reference fringe are fixed, an instantaneous change of air velocity produces a radial shift of the ring seen in the Rayleigh image. To measure the time variation of velocity, we must monitor the ring diameter in the Rayleigh image. To this end Seasholtz *et al.* (2001, 2002) used an image dissector that split the Rayleigh image into two concentric parts (figure 2*c*), and measured the ratio of light intensities from the inner and the outer parts using two photomultiplier tubes (PMTs). The ratio of photoelectron counts from the two PMTs carried information about the ring diameter variation in the Rayleigh image, which in turn reflects the change of Doppler shift frequency from velocity change at the probe volume. A calibration in a known flow field is necessary to relate intensity ratio to air velocity.

To measure density fluctuations, along with velocity fluctuations a small part of the Rayleigh scattered light delivered through the optical fibre was split off and the intensity fluctuations were monitored using a third photo-multiplier tube. The rest of the light was passed through the interferometer for velocity measurement as described above. For a fixed optical set-up and a fixed gas composition, the intensity variation of Rayleigh scattered light is directly proportional to air density variation (Panda &

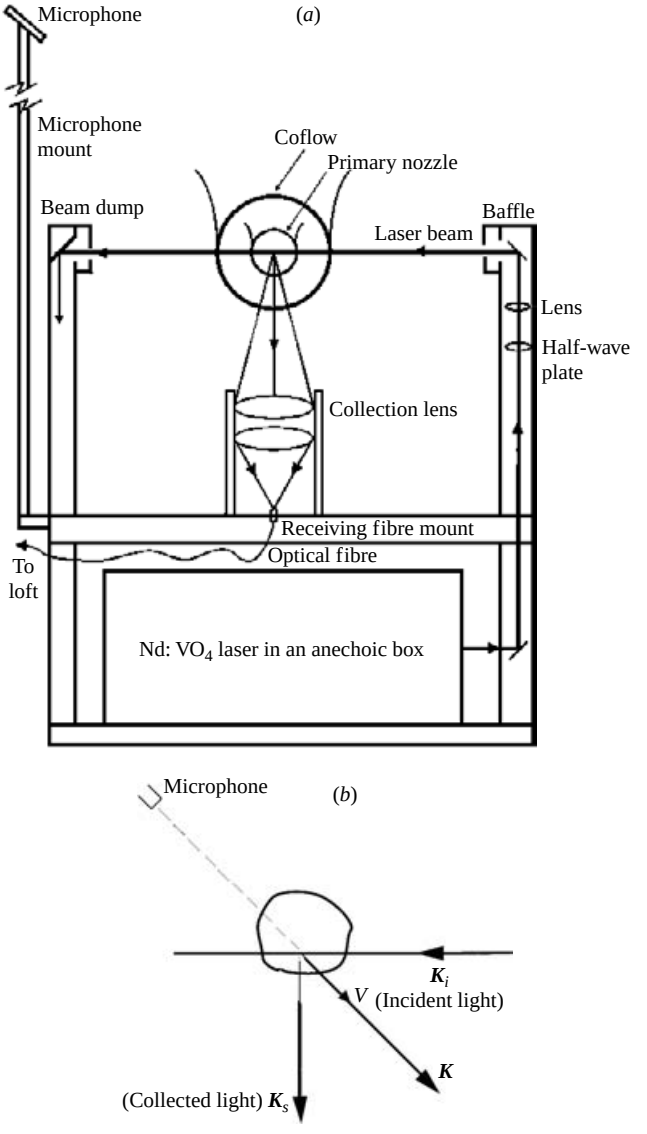

FIGURE 3(*a*, *b*). For caption see facing page.

Seasholtz 2002). Once again, a calibration is necessary to relate photo-electron count to density change. The calibration was performed in the same core regions of the jet flows used for velocity calibration. In summary, a total of three PMTs were used for simultaneous measurement of velocity and density fluctuations: two for measuring velocity and one for density. Additionally, two sets of calibration constants were required for velocity and density measurements in unknown flows.

The component of velocity measured using a given optical arrangement depends on the angular position of the collection lens with respect to the incident laser beam. Figure 3 shows two different optical arrangements of the transmission and collection optics for measuring the u and v velocity components. The Rayleigh scattered light was collected and transmitted to an adjoining room for spectral analysis. Figure 4 shows a schematic of the spectroscopic arrangement which was identical for both

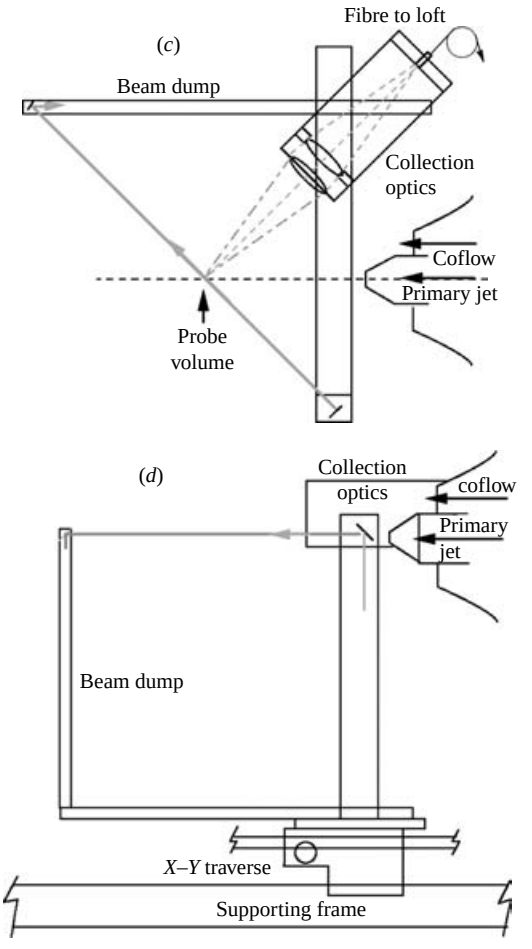

FIGURE 3. (*a*) Schematic of optical arrangement around jet facility to measure radial v component of velocity. (*b*) Scattering diagram for v measurement. (*c*) Top view of optical arrangement to measure axial u component. (*d*) Side view for u component measurement.

velocity components. Since density and one component of velocity were measured simultaneously, either $\rho(t)$ and $u(t)$ or $\rho(t)$ and $v(t)$ were measured using the two different collection arrangements. Figure 3(*b*) presents a scattering diagram pertinent to the radial v component measurement. $\boldsymbol{k}_i$ is the incident wave vector normal to the jet flow direction, $\boldsymbol{k}_s$ is the scattered wave vector pointing towards the collection optics and, $\boldsymbol{k} = \boldsymbol{k}_s - \boldsymbol{k}_i$, is the interaction vector. The arrangement measures Doppler shift, $f_d = \boldsymbol{k} \cdot \boldsymbol{U}/2\pi$ from the radial velocity component v, which is aligned along the interaction vector. A similar diagram for the optical arrangement of figure 3(*c*) shows that the measured Doppler shift corresponds to $-u$ component. The calibration process accounted for the sign reversal.

In addition to the optical frequency distribution of the scattered light, the image formed by the Fabry–Perot interferometer depends on properties of the interferometer: expressed via an instrument function $I_{FP}(\nu, \theta_{r'})$. The image formed, after the Rayleigh light is passed through a Fabry–Perot interferometer, is basically a product of the Rayleigh spectrum (equation (1)) with the instrument function. The light power

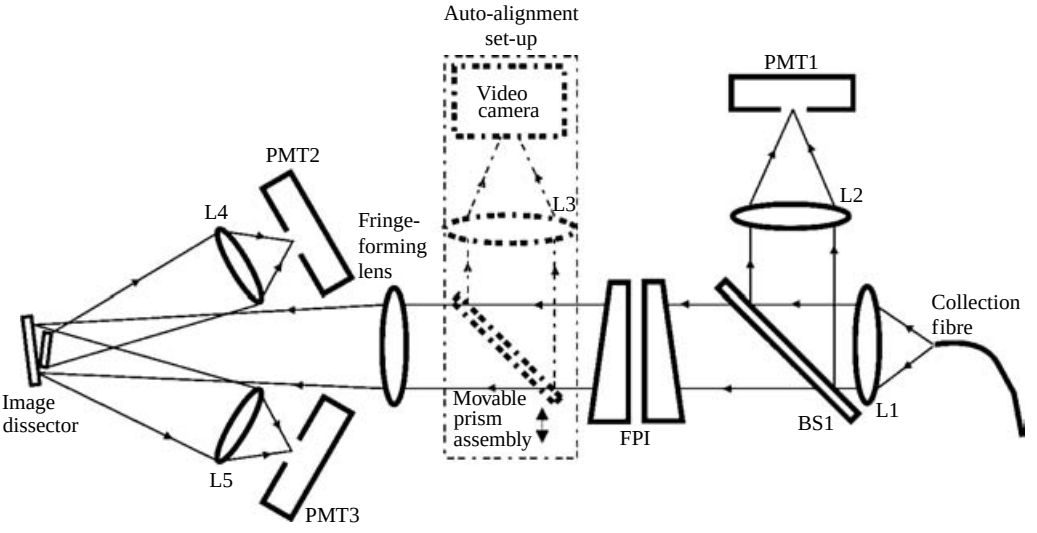

FIGURE 4. Schematic of optical set-up to analyse collected light. L1 to L5 are lenses; BS1 is a beam-splitter and FPI is the Fabry–Perot interferometer.

distribution P_I at any position $(r', \theta_{r'})$ in the image plane is given as:

$$P_I(r', \theta_{r'})\,\mathrm{d}A = P_{\Re} \int\int \Re(\nu)\, I_{FP}(\nu, \theta_{r'})\,\mathrm{d}\nu\,\mathrm{dA}, \tag{2}$$

where, $P_{\Re}$ is the total Rayleigh scattered power, and $\theta_{r'}$ is the angle made with optical axis by a light ray reaching the elementary area $\mathrm{d}A$ in the image plane. In the current set-up, this image, formed at the focal plane of the fringe-forming lens, was dissected into two parts by a concentric tilted mirror assembly (image dissector in figure 4) and measured by two PMTs. The intensity variations from the two parts were measured from known velocity flows. It was found that the intensity variations in either part of the image can be modelled by second-order polynomials. If N_2 and N_3 denote photo-electron count rates from the inner and outer PMTs then:

$$N_2 = A_i + uB_i + u^2C_i, \quad N_3 = A_o + uB_o + u^2C_o. \tag{3}$$

Where, A_i, B_i, C_i, A_o, B_o and C_o are calibration constants. The velocity component u is measured from a ratio of the two counts, $R = N_3/N_2$:

$$u = \frac{-(RB_i - B_o) + \sqrt{(RB_i - B_o)^2 - 4\,(RA_i - A_o)\,(RC_i - C_o)}}{2\,(RC_i - C_o)}. \tag{4}$$

Note that the ratio of two counts cancels out changes in overall scattering intensity associated with flow density variation. Also the physically meaningful, positive root of the quadratic equation is considered. An important caveat in the above analysis is an implicit assumption that the effect of temperature fluctuations is also accounted for via the calibration process. Temperature broadening results in changes of light intensity in both the inner and outer parts of the image. By virtue of measuring a ratio of intensities between the two parts of the image, the process was made somewhat insensitive to temperature fluctuations. A numerical uncertainty analysis (Seasholtz *et al.* 2001) demonstrates that the effect of temperature fluctuation is small compared to the bigger change associated with velocity fluctuations. In addition, the present experiment was conducted in the same unheated jets used to obtain

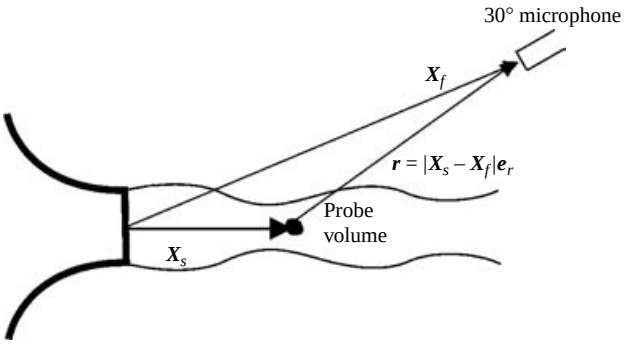

FIGURE 5. Schematic of coordinate system and microphone locations.

calibration constants. Hence, the influence of isentropic temperature fluctuations was automatically included in the calibration constant. However, non-isentropic temperature fluctuations from certain regions of the jet have affected the velocity fluctuations data in a small yet unknown way.

Density variations were measured by splitting off about 10 % of the collected light using a beam splitter (BS1 in figure 4) before the rest is passed through the interferometer. The power variation in this split part is measured by PMT1. It is known that for a fixed optical set-up and a fixed composition of gases, the total scattered light is directly proportional to the gas density: $P_{\Re} \propto \rho$. If the photo-electron count rate from PMT1 is N_1 then:

$$N_1 = C_{\rho 1} + \rho C_{\rho 2}, \tag{5}$$

where $C_{\rho 1}$ and $C_{\rho 2}$ are calibration constants determined from measurements in known density flows.

1.2. *Causality relation*

There follows a recollection of the principles behind the causality relation. More detailed discussion of the analytical steps can be found in Seiner (1974); also see Lee & Ribner (1972) and Siddon (1973). It should be mentioned at the outset that the purpose here is to help in the interpretation of the experimental data (unlike many previous workers, no effort was made to evaluate the volume integrals). In addition to the acoustic analogy route, the instability wave model proposed by Michalke (1977, 1983) and others, and large-scale–fine-scale distinction proposed by Tam (1998) are also used for more straightforward interpretation of the data. In fact, many experimental observations presented in this paper are supportive of the arguments proposed in these newer theories.

The causality relation is based on Lighthill's equation (1954) which, neglecting viscous terms, is the following:

$$\frac{\partial^2 \rho}{\partial t^2} - a_0^2 \nabla^2 \rho = \frac{\partial^2 T_{ij}}{\partial X_i \, \partial X_j}; \qquad T_{ij} = \rho U_i U_j + \delta_{ij}\big(p - a_0^2 \rho\big), \tag{6}$$

where ρ is air density, p is pressure, a_0 is ambient speed of sound, U_i and U_j are velocity vectors and T_{ij} are the elements of the stress tensor. The free-space solution for a field point $\boldsymbol{X}_f$ from distributed source points $\boldsymbol{X}_s$ (figure 5) is:

$$p'(\boldsymbol{X}_f; t) = \frac{1}{4\pi} \frac{\partial^2}{\partial X_i \partial X_j} \int_{\boldsymbol{V}} T_{ij}(\boldsymbol{X}_s; t') \frac{d^3 \boldsymbol{X}_s}{|\boldsymbol{X}_f - \boldsymbol{X}_s|} \tag{7}$$

Where, p' represents pressure fluctuations and the terms inside the integral are calculated at a retarded time to account for propagation from the source point to the field point: $t' = t - \tau_0$, $\tau_0 = |\boldsymbol{X}_f - \boldsymbol{X}_s|/a_0$. The integral is taken over the whole jet volume $\boldsymbol{V}$. Equation (6) shows that the stress tensor T_{ij} has two terms. The first term $\rho U_i U_j$ has nine different components; out of which the contribution from ρvv (v: radial component of velocity) and ρuu (u: axial component) fluctuations are measured in the present work. In the following, application of the causality relationship to the $\rho U_i U_j$ term is outlined. Various issues involved in the interpretation are discussed next. Contribution from the second term of the stress tensor, $(p - a_0^2\rho)$, requires fluctuation measurements of two different thermodynamic variables. The current technique measures one: density fluctuations. Therefore, the contribution from the second term could not be evaluated correctly.

Following Proudman's analysis (1952), the double space divergence can be converted into double time derivative under two restrictions: (a) a scalar component of the stress tensor must be measured along the direction of observation from the source, and (b) the field point is far enough to be in the radiation field of all sources. Under these conditions, the acoustic pressure at the field point can be written as:

$$p'(\boldsymbol{X}_f; t) = \frac{1}{4\pi a_0^2 \boldsymbol{r}} \int_{\boldsymbol{V}} \frac{\partial^2}{\partial t'^2} [\rho u_r u_r (\boldsymbol{X}_s; t')] \, \mathrm{d}^3 \boldsymbol{X}_s \tag{8}$$

where $\boldsymbol{r} = \boldsymbol{X}_f - \boldsymbol{X}_s$ is radial distance and u_r is the velocity component along the observer direction. The scalar components of the stress tensor represent longitudinal quadrupoles, made by on-axis positioning of two opposite dipoles. Such a quadrupole has very strong directivity and, in the absence of convective amplification, the acoustic intensity falls as the $\cos^4$ from the peak radiation direction. The peak radiation directions associated with quadrupoles, $\partial^2(\rho uu)/a_0^2 \partial t'^2$ and $\partial^2(\rho vv)/a_0^2 \partial t'^2$, are, respectively, along the jet axis and 90° to the axis. The former is affected by refraction and convective amplification while the latter is not.

To obtain acoustic intensity, an autocorrelation function for the above equation must be worked out. Usually, the autocorrelation function is created by multiplying space–time separated stress tensors separated in space by ξ and in time by τ:

$$\langle p'^2 \rangle (\boldsymbol{X}_f; \tau) = \frac{1}{16\pi^2 a_0^4 \boldsymbol{r}^2} \int_{\boldsymbol{\xi}} \int_{\boldsymbol{V}} \frac{\partial^4}{\partial t^4} \langle \rho u_r u_r (\boldsymbol{X}_s; t') \rho u_r u_r (\boldsymbol{X}_s + \boldsymbol{\xi}; t' + \tau) \rangle \, \mathrm{d}^3 \boldsymbol{X}_s \, \mathrm{d}\boldsymbol{\xi}. \tag{9}$$

In the 'causality' relationship, however, this is accomplished by multiplying the source integral with the far-field sound pressure:

$$\begin{aligned} \langle p'^2 \rangle (\boldsymbol{X}_f; \tau) &= \left\langle \left[\frac{1}{4\pi a_0^2 \boldsymbol{r}} \int_{\boldsymbol{V}} \frac{\partial^2}{\partial t'^2} [\rho u_r u_r (\boldsymbol{X}_s; t' + \tau)] \, \mathrm{d}^3 \boldsymbol{X}_s \right] [p'(\boldsymbol{X}_f; t)] \right\rangle \\ &= \frac{1}{4\pi \boldsymbol{r} a_0^2} \int_{\boldsymbol{V}} \frac{\partial^2}{\partial \tau^2} \left[R_{\rho u_r u_r; p'} (\boldsymbol{X}_s, \boldsymbol{X}_f; \tau) \right] \mathrm{d}^3 \boldsymbol{X}_s \end{aligned} \tag{10}$$

where $R_{\rho u_r u_r; p'}(\boldsymbol{X}_s, \boldsymbol{X}_f; \tau) = \langle \rho u_r u_r (\boldsymbol{X}_s; t + \tau - \tau_0) p'(\boldsymbol{X}_f; t) \rangle$.

The angle bracketed expressions imply time averages. Such time averages are also expressed with an additional semi-colon, e.g. $\langle \rho uu; p' \rangle$, in the text. The correlation function $R_{\rho u_r u_r; p'}$ has to be calculated after shifting the $\rho u_r u_r$ data by the propagation time $\tau = -\tau_0$, or inversely the pressure fluctuation data by $\tau = \tau_0$. In essence, (10) expresses the radiated acoustic field in terms of a time-delayed integral taken over the entire source volume, and consists of correlation functions between far-field sound pressure p' and source field $\rho u_r u_r$ fluctuations along the observer direction.

There is a particular advantage of (10) over (9). Lighthill's equation by itself is unable to separate hydrodynamic and acoustic fluctuations. The former is the pressure field associated with turbulent fluctuations, and the latter is the radiated fluctuations that propagate far away from the turbulent motion. Lighthill's equation is merely a reformulation of the mass and momentum conservation equations and therefore every solution upholds these two physical laws. It is known that only a small part of the disturbances created by turbulent motion ultimately radiates as sound. Since both radiating and non-radiating disturbances satisfy the same conservation laws, Lighthill's equation is unable to separate the two. Additional criteria are necessary, such as a frequency–wavenumber, ω–κ, analysis of the turbulent motion and imposition of a condition of supersonic convective speed with respect to the ambient sound speed: $\omega/\kappa \geqslant a_0$. The traditional autocorrelation function in (9) is created by correlating two source points. In order to determine which part of this correlation ultimately radiates as sound, an additional wavenumber–frequency analysis of the right-hand side is required (Goldstein 1976; Morris *et al.* 2002). On the other hand, multiplication by the fluctuations in the field point (equation (10)) effectively imposes a filter function since, by definition, a microphone kept in a far-field location only senses the radiated part of disturbances. Therefore, the cross-correlation function $R_{\rho u_r u_r; p'}$ separates hydrodynamic and acoustic fluctuations. There is no need to perform additional frequency–wavenumber analysis.

The causality relationship requires a second time-derivative, which ought to be avoided in experiments. Fourier transform of (10) yields (noting that the autocorrelation function is transformed to power spectral density and cross-correlation to cross-spectral density):

$$\left.\begin{aligned} S_{p'^2}(X_f; f)\,\mathrm{d}f &= -\frac{\pi f^2\,\mathrm{d}f}{r a_0^2}\int_{\boldsymbol{V}} S_{\rho u_r u_r, p'}(X_f, X_s; f)\,\mathrm{d}^3 X_x, \\ \text{cross-spectrum:}\quad S_{\rho u_r u_r, p'}(X_f, X_s; f) &= \int_{-\infty}^{\infty} R_{\rho u_r u_r; p'}(X_s, X_f; \tau)\exp(-j2\pi f\tau)\,\mathrm{d}\tau. \end{aligned}\right\} \tag{11}$$

Finally, the acoustic intensity at the field point $\boldsymbol{X}_f$:

$$I(X_f) = \frac{1}{a_0\rho_0}\int_{-\infty}^{\infty} S_{p'^2}\,\mathrm{d}f = -\frac{\pi}{r\rho_0 a_0^3}\int_{-\infty}^{\infty}\int_{\boldsymbol{V}} f^2 S_{\rho u_r u_r, p'}(X_f, X_s; f)\,\mathrm{d}^3 X_s\,\mathrm{d}f. \tag{12}$$

Equation (12) shows that the intensity of sound radiation is directly dependent on the distribution of cross-spectral density function in the flow field.

There are multiple issues surrounding the causality method. At first glance, the right-hand sides of (9) and (10) are expected to be equal, although the integrands are different. However, they may not be so, as the difference between propagating and non-propagating disturbances is included in the latter. There is an issue of non-uniqueness in the application of the causality method (Ffowcs Williams 1973). Since the sound pressure at the field point is a large sum over the entire sound-producing region of the jet, an unlimited number of variations in the source correlation can lead to the same summation at the field point. This criticism is not special for the causality technique, but is in general true for the more common form of source description via two-source points correlation (equation (9)), which likewise, has to be integrated over the source volume. In a broader sense, many inverse problems in physics are of this nature. Although mathematically this appears to be a problem, it can be argued that the distribution of correlation functions measured in a real experiment is the valid distribution.

The interpretation of the correlation function is another issue. If the sound producing eddies are uncorrelated, as in the high-frequency components, then the $\langle \rho u_r u_r, p' \rangle$ correlation function measured from various points in the jet are mutually independent; the integration over the jet volume becomes a simple addition in power and the correlation data can be used to determine source efficiency along the jet axis (Seiner & Reethof 1974). Such an interpretation also leads to a discussion of the number of eddies responsible for sound generation at a given instant (Lee & Ribner 1972). It is now well established from various experimental observations that low-Strouhal-frequency turbulent fluctuations are dominated by organized vortical waves with significantly long spatial coherence. The effect of source-coherence on jet noise has been discussed by Michalke (1983). For sources with long spatial coherence, the phase of $\langle \rho u_r u_r, p' \rangle$ correlation will vary from point to point, and the integration over the jet volume requires a knowledge of both magnitude and phase.

The present paper makes only a limited effort to calculate far-field spectra from the measured correlations. One difficulty is that the requirement to measure the velocity component u_r along the observer direction was not always satisfied. For the 90° noise, the source term $\rho u_r u_r\,(=\rho vv)$ could be measured correctly from the radial v component data; however, for all other polar angles, the stress component can only be approximated from ρuu and ρvv measurements. Note that u and v components were measured separately at different times. It is best to present the experimental data in a non-dimensionalized form. Following the traditional acoustic analogy approach, two different velocity scales are applied: ambient sound speed a_0 for field points and U_j for source points. The length and time scales are derived using the jet diameter D and velocity scales. The ambient value ρ_0 is used to normalize density. Using superscript * for non-dimensionalized quantities, S_t for Strouhal number, and M_a for Mach number based on ambient sound speed, equation (11), for an observer located 90° to the jet axis, becomes:

$$\left.\begin{aligned} S^*_{p'^2}(\boldsymbol{X}^*_f; S_t)\,\mathrm{d}S_t &= -M_a^4 \frac{\pi S_t^2}{r^*}\,\mathrm{d}S_t \int_V S^*_{\rho vv,p'}(\boldsymbol{X}^*_f, \boldsymbol{X}^*_s; S_t)\,\mathrm{d}^3\boldsymbol{X}^*_s, \\ S_t = \frac{fD}{U_j}, \quad M_a = \frac{U_j}{a_0}, \quad S^*_{p'^2} &= \frac{S_{p'^2}}{\left(\rho_0 a_0^2\right)^2}, \quad S^*_{\rho vv,p'} = \frac{S_{\rho vv,p'}}{\left(\rho_0 U_j^2\right)\left(\rho_0 a_0^2\right)}. \end{aligned}\right\} \tag{13}$$

In the present experimental program the principal idea of correlating flow fluctuations to the sound pressure fluctuations has been extended to include some other variables, which do not necessarily abide by the framework of Lighthill's equation. For example, efforts are made to correlate ρvv fluctuations not only with the microphone signal from 90° to jet axis, but to the 30° position as well. Enquires are made as to how various other quantities, such as different Reynolds decomposed terms of ρuu: $\bar{\rho}\bar{u}u'$, $\rho'\bar{u}u'$, etc. correlate with sound pressure fluctuations. Additionally, comparisons are made between correlations from density fluctuations and velocity fluctuations with a fixed microphone signal. These additional efforts resulted in some interesting results.

2. Experimental set-up

Experiments were performed at NASA Glenn Research Center using three different nozzles (one convergent and two convergent–divergent) operated at Mach numbers, $M = 0.95$, 1.4 and 1.8. The convergent–divergent nozzles were designed by the method of characteristics. The operating conditions are described in table 1. All nozzles were

Specific heat ratio, $\gamma = 1.4$; Total temperature, $T_0 = 300\,\mathrm{K}$; Ambient density, $\rho_0 = 1.16\,\mathrm{kg\,m^{-3}}$, Ambient sound speed, $a_0 = 347\,\mathrm{m\,s^{-1}}$

Nozzle type	Convergent operated at $M = 0.95$	M 1.4 CD	M 1.8 CD
Minimum shock operation at $M =$		1.395	1.795
Reynolds number Re_D	0.66×10^6	1.16×10^6	1.88×10^6
Jet velocity U_j ($\mathrm{m\,s^{-1}}$)	316	411	486
Estimated eddy convection speed U_c ($\mathrm{m\,s^{-1}}$) $= 0.6U_j$–$0.89U_j$	190–282	247–366	292–433
Jet density ρ_j ($\mathrm{kg\,m^{-3}}$)	1.36	1.6	1.89
Frequency (kHz) for $St = 1$	12.4	16.2	19.1

TABLE 1. Nominal operating conditions.

25.4 mm in exit diameter. The jet facility used a continuous supply of unheated compressed air. The facility was located in a large test chamber, which was not anechoic *per se*, but acoustic absorbent material was placed around the vicinity of the nozzle and in the ceiling and walls of the test cell to minimize reflection. Two 1/4-inch microphones were used to measure sound pressure fluctuation spectra. The microphones were mounted on an arc that allowed positioning at a distance of 50 diameters from the nozzle lip, and polar angles from 30° to 90° to the jet axis with 10° increments. For the bulk of the experiment, one of the microphones was kept fixed at 30° to the jet flow direction and the other at 90°. The Rayleigh-scattering system is somewhat elaborate and the following provides a brief description of some of the central features. An in-depth discussion of the Rayleigh set-up can be found in Seasholtz *et al.* (2001, 2002). The optical system was built in two parts. The first one is around the jet facility for transmitting laser light and collecting the scattered light (figure 3). The scattered light was then passed through a 0.55 mm diameter optical fibre to a quiet room where the second part, consisting of a spectroscopic system and photon counting electronics, were placed (figure 4). The splitting of the set-up is necessary to minimize the effect of vibration on the optical components. Additional care had to be taken to reduce dust particles in air streams, and to stabilize the interferometer from temperature and vibration induced drifts. To reduce dust particles, the dry air, supplied to the facility from a central high-pressure facility, was passed through additional micrometre sized filters which made the primary jet air very clean. To clean the entrained ambient air, an additional air blower and filter system was installed that provided a large 200 mm diameter low-speed ($\sim 20\,\mathrm{m\,s^{-1}}$) co-flow around the 25.4 mm primary jet.

There were two different optical systems built around the same jet facility to measure u and v components. Both of these were built over an X–Y traversing unit that carried laser head, transmission and collection optics. Surveys were made by moving the probe volume from point to point in the plume. The laser head of the solid-state frequency-doubled $Nd{:}VO_4$ laser was placed at the bottom part of the set-up (figure 3*a*). About 5 W of single mode 532 nm wavelength laser light was transmitted through a hollow side beam that contained a half-wave plate, focusing lens, mirrors and baffles. Since Rayleigh-scattered light is polarization dependent, the half-wave plate was rotated to align the peak scattering plane with receiving optics. The background scattered laser light was significantly attenuated by suitable use of baffles and beam-dump. It was found that the noise from the jet created a tonal excitement of the laser line at around 430 Hz. To reduce this excitation, an anechoic box was built around the laser

head. This box significantly reduced the laser unsteadiness, but a trace remained and manifested itself in the experimental results. The incident laser path and position of the collection optics differed for the two set-ups to measure radial (figure 3*a*) and axial (figure 3*c*, *d*) velocity components. For the former, the laser beam was passed normal to the jet axis and the collection optics were placed vertically down to collect scattered light from 90° to the incident beam as well as the jet axis. On the other hand, to measure the axial velocity component, the laser beam was passed at 45° to the jet axis, and 90° scattered light was collected by lenses oriented in the same plane containing the laser beam and the jet axis. The collection optics were the same for both set-ups. The scattered light was first collimated by a 300 mm focal length, 82 mm diameter achromat, and then focused by a 160 mm focal length achromat on the face of a 0.55 mm diameter multimode fibre. The combination of the fibre diameter and the magnification ratio of the collection optics defined the probe volume length to 1.03 mm. Not shown in figure 3 is an additional part of the set-up where a small part of light from the transmitting laser beam was split off for the purpose of monitoring laser frequency as well as to maintain the alignment in the Fabry–Perot interferometer. Whenever necessary, a pneumatically actuated mirror was placed in the transmission laser path to divert light towards a diffuser. The diffuser blocked Rayleigh-scatterded light yet scattered the diverted laser beam, which was then collected by the optical fibre.

The second part of the set-up is schematically shown in figure 4. Light arriving via an optical fibre was collimated by 100 mm focal length lens L1, and about 10 % was split by BS1 and measured by PMT1. Output from PMT1 provided information on the modulation of total scattered light intensity and therefore, was proportional to the air density fluctuations. The rest of the collimated beam was passed through a 70 mm aperture Fabry–Perot interferometer for spectral analysis. Single wavelength light from an extended source is imaged as concentric rings (fringes) at the output of the interferometer. However, restriction of the field of view, imposed by the fibre diameter, created only one fringe as shown earlier in figure 2. The fringe-forming lens, which ultimately images the fibre face on the image dissector, was made of two camera lenses with suitable separation for an effective focal length of 2909 mm. The large magnification ratio of the set-up created a 16 mm diameter image of the 0.55 mm diameter fibre on an image dissector. The image dissector was made of two concentric, and slightly tilted mirrors. The inner one had a diameter of 10 mm and directed the inner part of the fringe to PMT2, while the 25 mm diameter outer one directed the outer part of the fringe to PMT3. The ratio of light intensities from PMT2 and PMT3 provided a measure of either axial or radial velocity as described earlier.

The success of the velocity measurement system was critically dependent on stable operation of the interferometer. Slight thermal drift or change in the incident laser frequency displaced the reference fringe (figure 2*a*), which was manifested as an artificial bias in velocity measurement. This made the auto-alignment set-up (figure 4) necessary. The alignment system was a feedback control that first measured the reference fringe diameter and compared it with a prescribed targeted diameter. This was accomplished by splitting parts of the transmitted light using a three-prism assembly, and imaging them on a CCD camera. Subsequently, the difference between the targeted and the measured fringe diameters was translated into a change of high-voltage supply to the piezoelectric actuators that adjusted interferometer's plate separation. Before every Rayleigh measurement, reference light was collected and the auto-alignment system was engaged. When the desired fringe diameter was obtained

within a tolerance, the reference light collection system was disengaged, and velocity and density measurement via analysis of Rayleigh scattered light began.

Photoelectron-counting electronics were used with all 3 PMT signals. The photoelectron pulses from each PMT were first passed to a preamplifier (50 Ω impedance, $5\times$ gain) and then to a constant fraction discriminator (CFD) that provided a TTL level pulse for each photon pulse. The number of TTL pulses arriving within a preset gated time interval was counted using a PC counter-timer board. Counting was performed on a contiguous series of gated time intervals without any dead time between the gates. A digital I/O board provided the required clock pulses for gate generation. Pulses could be simultaneously counted on the three channels for indefinite times. Clock pulses from the same digital I/O board were also used to digitize microphone signal. Photo-electron counting was started at the beginning of a clock pulse that also digitized the analogue microphone signal; thereby assuring synchronization between three channels of photoelectron count and one channel of microphone signal digitization. The process was repeated for each of the microphone polar position. Long time records of up to 5 million data points from each PMT and the microphone channel were acquired with a typical sampling rate of $90\,000\,\mathrm{s}^{-1}$. The data points were converted to physical parameters: instantaneous density, velocity and sound pressure through the use of proper calibration constants. The Welch method of modified Periodograms (Welch 1967) was used to calculate individual power spectra and cross-spectra. Each long record was divided into small, 50 % overlapped, segments; modified periodograms of each segment provided local estimates; average of all local estimates provided the final power and cross-spectra. Time domain correlation calculations were also performed via Fourier transform, where individual segments of velocity and sound pressure time histories were Fourier transformed, multiplied and inverse transformed. Average of local estimates produced the final correlation. The length of the data segment was varied to assure independency of the calculated values on string length. More details on correlation calculation can be found in Panda & Seasholtz (2002).

3. Results

3.1. *Calibration and validation*

As described above, calibration constants are required to convert photo-electron counts from the three PMTs to density and velocity values. For this purpose, measurements had to be made in known velocity and density flows. The axial velocity and density in the potential core of jet plumes from a convergent nozzle operated in the subsonic Mach numbers, and CD nozzles at the correct operating conditions, are known from isentropic relations:

$$\rho = \frac{P_p}{RT_p}\left(\frac{P_p}{P_0}\right)^{-1/\gamma}; \quad u = Ma$$
$$\text{where} \quad M = \left[\left(\left(\frac{P_p}{P_0}\right)^{(\gamma-1)/\gamma} - 1\right)\frac{2}{\gamma-1}\right]^{0.5}, \quad a = \sqrt{\gamma RT_p}\left(\frac{P_p}{P_0}\right)^{(1-\gamma)/2\gamma}. \tag{14}$$

The ambient pressure P_0, plenum pressure P_p and plenum temperature T_p were monitored using pressure-transducers and a thermocouple. The specific heat ratio γ for unheated air is 1.4. Since the jets exhausted into ambient air, the plenum pressure was changed to vary plume Mach number. Axial velocity calibrations were performed in the same plumes where later measurements were performed. For the calibration of

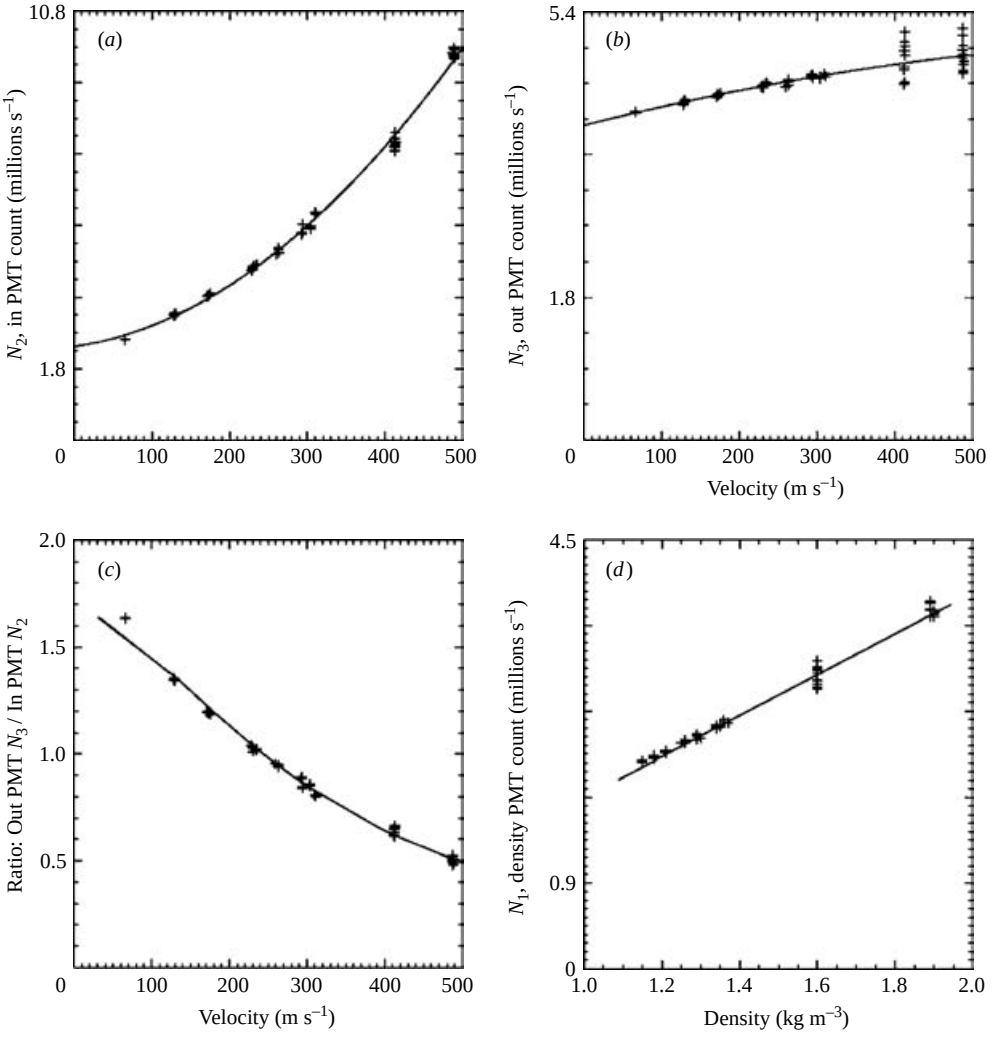

FIGURE 6. Density and velocity calibration using three photo-multiplier tubes.

the radial component of velocity, however, a separate small nozzle was mounted close to the probe volume. This calibration jet was rotated to align the plume along the radial velocity direction of the primary jet. Figure 6 shows a set of typical calibration curves for density and axial velocity measurements. Figures 6(*a*) and 6(*b*) show variations of count rate from the two PMTs that measure light intensities from the split images formed after the interferometer (PMT2 and PMT3 in figure 4). The solid lines are the least-squares fit of second-order polynomials as described in (3). Figure 6(*c*) shows the ratio of the two counts, measured at different flow velocities along with a solid line representing calculated velocities (equation (4)). This plot shows a reasonably good fit to the experimental data. Finally, density calibration is shown in figure 6(*d*). One noticeable feature is the relatively high scatter of the calibration data from the supersonic Mach 1.4 and 1.8 plumes. Prior density measurements and schlieren photographs in these plumes (Panda & Seasholtz 2002) showed the presence of weak shock structures even at the design operating condition. Perhaps weak shocks

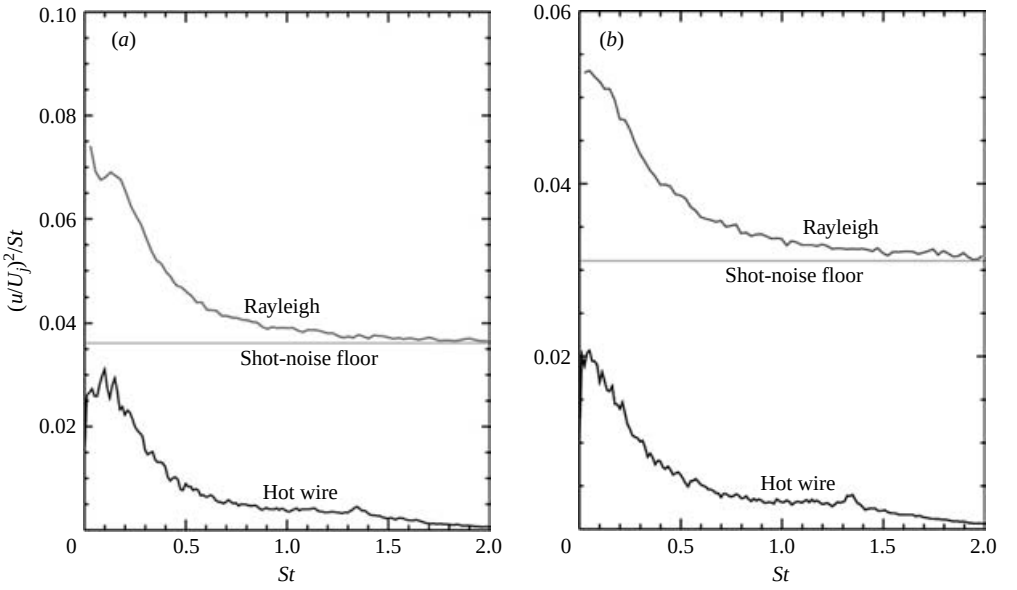

FIGURE 7. A comparison of power spectral density of u fluctuations measured by the Rayleigh technique and a hot-wire probe in the Mach 0.6 plume. (a) $x/D = 6$, $r/D = 0.5$; (b) $x/D = 10$, $r/D = 0$.

are impossible to avoid in any free supersonic shear flows. To average out the density and velocity variations across the periodic shock system, data were obtained from various axial stations within the potential core. The data scatter of figure 6 is a reflection of point-to-point variation in the supersonic plume.

Naturally, this data scatter has added some uncertainty in determining turbulent properties. There were additional minor sources; however, the combined effect of all such sources was masked by the uncertainty from electronic shot noise, inevitable in any optical intensity measurement. This is illustrated in figure 7 where velocity fluctuations spectra measured using the present Rayleigh arrangement is compared with that obtained using a hot-wire probe. This figure shows that the shapes of velocity spectra are similar while the absolute energy level in the spectrum measured by the Rayleigh technique is two and a half times that measured by hot wire. The Rayleigh spectra float on constant white-noise floors, which are expected consequences of electronic shot noise. The propagation of electronic shot noise in the velocity spectrum is somewhat complicated by the ratio of photoelectron counts, $R = N_3/N_2$, required to determine instantaneous velocity. The shot noise randomly changes the ratio and manifests as a noise floor in the velocity spectrum. This constant floor is all that exists in data taken from still ambient air. It should be mentioned that the primary interest of the present work is in cross-correlation between sound pressure fluctuations and turbulent flow fluctuations. Since the noise sources in the two measurements are different, the cross-correlation process eliminates the influence of electronic shot noise and the absolute cross-correlation values are expected to have a much smaller level of uncertainty.

Nevertheless, a reasonable estimate of the standard deviation (root-mean-square) of various fluctuating quantities is required to non-dimensionalize the absolute correlation values. For example, correlations between velocity fluctuations and far

field sound pressure fluctuations are expressed as $\langle u\,;p'\rangle/u_{rms}p_{rms}$, which requires an estimate of u_{rms}. Such root-mean-square or standard deviation was estimated from the individual spectra by noting that the total spectral energy is a sum of mean-square of velocity fluctuations u_{rms}^2 and that of shot noise σ_{shot}^2 (Saleh & Teich 1991):

$$\int S_{u^2}\,\mathrm{d}f = u_{rms}^2 + \sigma_{shot}^2. \tag{15}$$

Here, S_{u^2} represents power spectral density of u fluctuations measured in $(\mathrm{m\,s^{-1}})^2/\mathrm{Hz}$. Shot noise produces a frequency-independent white-noise level in the spectrum. This constant level was estimated as the spectral density value at the highest resolved frequency of 45 kHz: $S_{shot} = (S_{u^2})_{f=45000}$ where it is known that the energy from turbulent fluctuations is small.

$$u_{rms} = \sqrt{\int [S_{u^2} - (S_{u^2})_{f=45000}]\,\mathrm{d}f}. \tag{16}$$

The r.m.s. values measured by this shot noise subtraction process are found to be reasonable. For example, in figure 7(*a*), $(u_{rms}/U_j)_{hot\text{-}wire} = 0.166$ and $(u_{rms}/U_j)_{Rayleigh\ corrected} = 0.154$ and in figure 7(*b*) $(u_{rms}/U_j)_{hot\text{-}wire} = 0.14$ and $(u_{rms}/U_j)_{Rayleigh\ corrected} = 0.132$. The subtraction method was used uniformly to estimate $\rho_{rms,}\ u_{rms}$ and $(\rho uu)_{rms}$ from the respective spectra.

3.2. *Density and velocity fluctuations spectra*

Figure 8 shows typical velocity and density spectra obtained from the strongest noise-generating regions of a Mach 1.4 plume. All velocity data is non-dimensionalized by the centreline axial velocity U_j, while density is non-dimensionalized by the ambient value. The digital power spectral calculations provided mean-square fluctuations within a frequency band Δf for different centre frequencies f_c. Since the centre frequencies were converted to Strouhal numbers, the same was applied to Δf to obtain $\Delta St = \Delta f\,D/U_j$, and then divided the spectra by that number to obtain the power spectral density.

The ρuu spectrum of figure 8(*d*) was obtained by first multiplying instantaneous density and velocity: $\rho uu(t) = \rho(t)u(t)u(t)$, and then taking Fourier transforms of the resulting time series data. The density velocity cross-spectrum was obtained by multiplying Fourier transform of individual time traces:

$$\left.\begin{aligned} &S_{u\rho}(f) = \mathfrak{F}(\rho(t)) * \mathfrak{F}^*(u(t)) = Re\{S_{u\rho}\} - \mathrm{i}\mathrm{Im}\{S_{u\rho}\} \\ &\text{magnitude } |S_{u\rho}| = \sqrt{(\mathrm{Re}\{S_{u\rho}\})^2 + (\mathrm{Im}\{S_{u\rho}\})^2}, \quad \text{phase } \theta_{u\rho} = \frac{\mathrm{Im}\{S_{u\rho}\}}{\mathrm{Re}\{S_{u\rho}\}}. \end{aligned}\right\} \tag{17}$$

In this equation, complex conjugation is represented by the superscript $*$ and Fourier transformation by $\mathfrak{F}$. The magnitude of the cross-spectral density is plotted in figure 8(*e*), and the phase in 8(*f*). Note that the sharp spike at very low Strouhal frequency (430 Hz in absolute frequency) is due to a spurious oscillation in the laser frequency and should be ignored. The spike is not due to any tone produced by the jet. None of the jet operating conditions produced any tone – this was confirmed from multitudes of microphone spectra collected from all operating conditions. Moreover, the spike frequency was independent of jet speed; an increase in velocity only increased the spectral level of the spike, keeping the frequency intact. It has been mentioned earlier that a semi-anechoic chamber was built around the laser head as a protection from high noise produced by the jets. In the absence of the anechoic chamber,

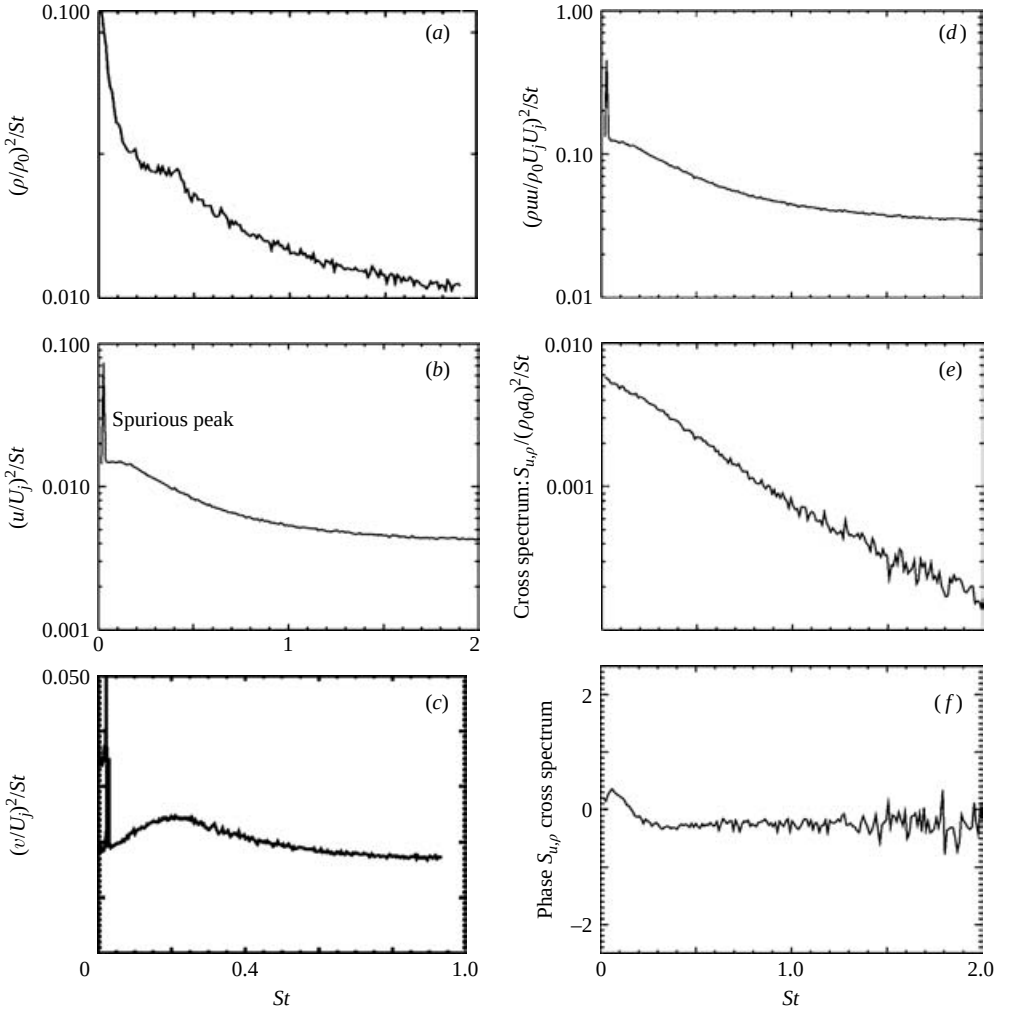

FIGURE 8. Power spectral density of (*a*) air density, (*b*) axial velocity, (*c*) radial velocity, (*d*) density* (axial velocity)^2 fluctuations; (*e*) magnitude of density-axial velocity cross-spectrum, and (*f*) phase of cross-spectrum in the Mach 1.4 jet at centreline and $x/D = 10$.

the energy level in the spike increased many times. Therefore, the semi-anechoic chamber was effective, albeit partially, in reducing the noise level felt by the laser. It is believed that either the laser cavity or one of the sensitive optics inside the laser head was mechanically responding to the noise. This caused a small variation in laser frequency, which in turn pulsated slightly the image formed by the interferometer. The final outcome is the spurious spike in the velocity and other related spectra.

It is possible to make multiple observations from figure 8. (i) The density fluctuation spectrum is similar to that of the axial velocity spectrum, while the radial velocity spectrum shows some difference: the u and ρ spectra show a continuously decaying shape, while the v-spectrum has a hump shape. This indicates a difference in eddies that produce the most energetic fluctuations in axial and radial velocity components. However, data obtained from the shear layer show similarity in shapes for all three spectra: ρ, u and v. That the density fluctuation spectra follows that of the

axial velocity is expected, as u fluctuations are more energetic than v fluctuations. The difference between u and v spectra, however, is unexpected. In the normal mode representation of turbulent fluctuations, which is commonly employed in hydrodynamic stability calculations, it is customary to assume identical spectral distribution for all flow and thermodynamic variables. The experimental data, at least around the strongest noise producing centreline region of the jet, does not support this model. (ii) From figure 8, the ρuu spectrum, as expected, has the same shape as that of u spectrum, although in absolute value $(\rho uu)_{rms} \gg u_{rms}$. (iii) The velocity–density cross-spectrum has a continuously decaying shape, indicating u and ρ fluctuations are best correlated in the larger lower-frequency eddies and progressively decorrelate as the eddy size becomes smaller. (iv) The flat phase relation of figure 8(f) implies that density and axial velocity fluctuations are in phase for all eddy sizes. A discussion of measurement uncertainties follows.

As already mentioned, the fundamental source of uncertainty in optical measurement is due to electronic shot noise which adds a constant floor to the spectrum. The constant noise floor particularly masks the lower-energy high-frequency side of the spectrum. It is estimated that as much as 50 % of spectral energy at $St = 0.2$ may be due to this electronic noise source. The second source of uncertainty is due to a slow random variation in the laser frequency over 30 MHz (0.001 cm^{-1}) that translates into $\pm 8\,\mathrm{m\,s}^{-1}$ velocity fluctuation. The third source is due to the excitation of laser cavity by jet noise that manifests in the 430 Hz peak in u, v, ρuu spectra. Finally, the Fabry–Perot stabilization set-up, required to lock the reference fringe at a fixed radial position, was effective only within an error margin. A change in the reference fringe position, from the value used for calibration, translates into a spurious mean velocity in the analysed signal. Similarly, a random positioning error in the reference fringe results in added energy in the spectral data. A direct estimate of the uncertainty from all such sources is difficult to obtain. Nevertheless, the success of the causality method is critically hinged on noise cancellation obtained in cross-correlating two signals of independent noise sources. This cross-correlation is described in the next section.

3.3. *Correlation between flow fluctuations and sound pressure fluctuations*

The presentation of correlation data starts with figure 9, where normalized cross-correlation data from 30° and 90° microphone polar angles are presented. The cross-correlation values were calculated via Fourier transform, that is, the cross-spectrum was calculated first, and then an inverse transform was taken to return to the time domain. Long data segments were used for the calculation: neither the flow data, nor the microphone data were shifted in time. The cross-correlation data show sharp rises at a time delay which corresponds to the time required for sound waves to travel from the laser probe location to the microphone location, $\tau_0 = \boldsymbol{r}/a_0$. This confirms that the turbulent fluctuations are indeed producing the sound pressure fluctuations at a predictable time lag, and in turn provides confidence in the measurements. Figure 9 presents data from the axial velocity u set-up. The laser probe was located at the centreline and farther downstream from the end of the potential core: a region found to be the strongest sound source. There are multiple observations that can be made from figure 9. (i) Air density fluctuations show as good a correlation as ρuu. (ii) Sound pressure fluctuations at 90° to the jet axis correlate poorly with any flow variables. (iii) The time duration $\Delta\tau$ over which correlation changes from zero to negative to positive and back to zero is significantly long (figure 9c). The microphone signal is responding to long durations of turbulent fluctuations in the probe volume. Since the turbulence is convected with the flow, $\Delta\tau$ is related to the spatial extent of

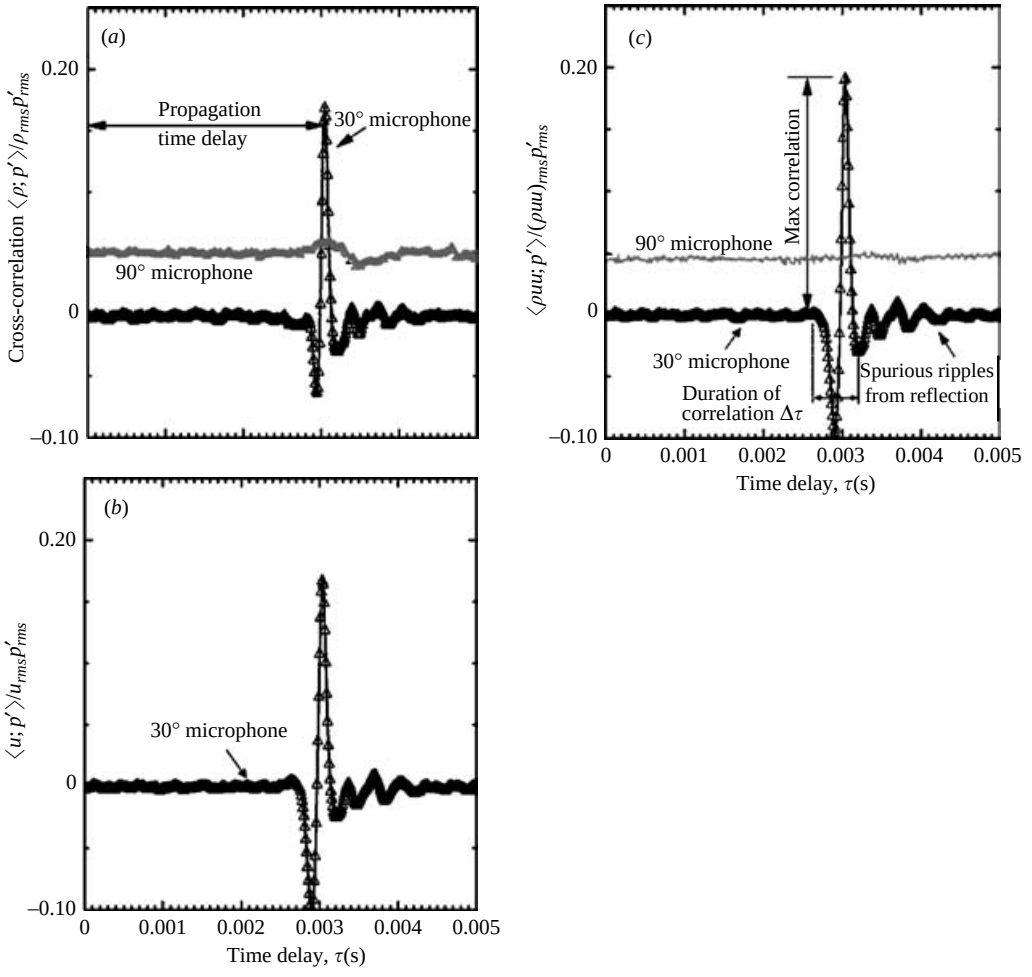

FIGURE 9. Normalized cross-correlation between sound pressure fluctuations p' and (*a*) air density ρ, (*b*) axial velocity u and (*c*) ρuu fluctuations measured at $x/D = 10$ and centreline of $M = 1.4$ jet. The microphone was kept at $50D$ and at the indicated polar angles. The 90° microphone data is shifted by 0.05.

the source. The trailing edge of the correlation is somewhat difficult to determine; nevertheless for the particular jet, $\Delta\tau$ is estimated as 0.53 ms. This provides a measure of coherence time of the dynamic process responsible for sound radiation. Invoking Taylor's hypothesis, the corresponding coherence length scale is $l_{coher} = \Delta\tau U_c$, where U_c is the convective speed. Assuming $U_c = 0.7U_j$, the coherence length $l_{coher} \approx 6D$. In other words, the longest source contributing towards correlation is, on average, 6 jet diameters long. Therefore, the noise source responsible for sound radiation, at the shallow 30° angle, is indeed 'non-compact'. A discussion of uncertainty in correlation data follows.

As mentioned earlier, the cross-correlation process significantly reduces the shot noise contribution and therefore absolute values of $\langle \rho; p' \rangle$ and $\langle \rho uu; p' \rangle$ are relatively error free. The primary source of uncertainty is the shot noise elimination process used

in estimating root-mean-square values: ρ_{rms}, $(\rho uu)_{rms}$ etc. The shot-noise subtraction process has been described earlier. From repeated measurements and comparison with hot-wire data it is estimated that there is a $\pm 10\,\%$ uncertainty in r.m.s. calculation, which produces an equal uncertainty in correlation data. A second source of uncertainty is sound reflection from large lenses placed close to the plume. Although most of the optical components and mounts were covered by polyurethane foam to minimize reflection, some could not be covered for obvious reasons. The reflected sound waves arrive at the microphone position at a longer time delay than those reaching directly from the source. The additional ripples after the large primary spike, seen in figure 9, are due to the delayed reflected waves. For most cases, it is easy to separate out the spurious reflected part from the desired direct correlation and it is expected to have minimum effect on the maximum correlation value.

3.4. *Reynolds decomposition of ρuu and correlation with sound pressure fluctuations*

The largest term in the Lighthill stress tensor arises from ρuu fluctuations, and figure 9 confirms that indeed the highest correlation is measured from this quantity. From the modelling perspective, it is of interest to break down the full flux term into time-averaged and fluctuating parts and to see how the individual components correlate with the far-field noise:

$$\left.\begin{aligned} &\rho = \bar{\rho} + \rho', \quad u = \bar{u} + u', \\ &\langle \rho uu\,; p' \rangle = \langle 2\bar{\rho}\bar{u}u'\,; p' \rangle + \langle \rho'\bar{u}\bar{u}\,; p' \rangle + \langle 2\bar{u}\rho'u'\,; p' \rangle + \langle \bar{\rho}u'u'\,; p' \rangle + \langle \rho'u'u'\,; p' \rangle. \end{aligned}\right\} \tag{18}$$

The five fluctuating terms in ρuu decomposition were constructed from the measured $\rho(t), u(t)$ time traces and individually correlated with the sound pressure fluctuations from the 30° microphone. Figure 10 presents this data along with correlation from the full ρuu term. To help interpretation, correlation data must be normalized by a product of standard deviation of sound pressure fluctuations and standard deviation of turbulent fluctuations. There are two choices for the latter: either to use the same $(\rho uu)_{rms}$ for all terms, or to use standard deviation for the individual fluctuating terms, e.g. $(\rho'\bar{u}\bar{u})_{rms}$, $(2\bar{\rho}\,\bar{u}u')_{rms}$ etc. The first choice provides a uniform comparative basis, while the second may be more meaningful. Figure 10 presents correlation data normalized by both means. The numerical values of the peak correlation coefficients for many jet operating conditions are provided in table 2. A closer examination of figure 10 and table 2 reveals some interesting observations. (i) Correlation data, uniformly normalized by $(\rho uu)_{rms}p'_{rms}$, show that the largest contribution is from the 'shear noise' term $2\bar{\rho}\bar{u}u'$, and the next important term is $\rho'\bar{u}\bar{u}$: the other first-order term. The terms which are second- and third order in fluctuations contribute minimally. That the self noise $\langle 2\bar{u}u'\,; p' \rangle$ is higher than shear noise $\langle u'u'\,; p' \rangle$ is consistent with many prior observations (Lee & Ribner 1972; Seiner 1974 among others). However, when the same data set is normalized by the standard deviation of individual fluctuating components, correlation due to the third-order term, $\rho'u'u'$, becomes as important as the first-order. Traditionally, this term has been ignored in the noise models. (ii) Figure 10 shows that the time sequence of correlation, zero to negative to positive and back to zero, is different between first-, second- and third-order terms. The minimum appears before the maximum in $\langle 2\bar{\rho}\bar{u}u'\,; p' \rangle$ correlation, while it is reversed in $\langle 2\bar{\rho}u'u'\,; p' \rangle$ correlation. In general, correlation with first- and third-order terms are nearly in phase, while the second-order terms are opposite in phase. Therefore, a simple sum of the positive maxima values in the constituent correlations do not add up to value measured in $\langle \rho uu\,; p' \rangle$ correlation.

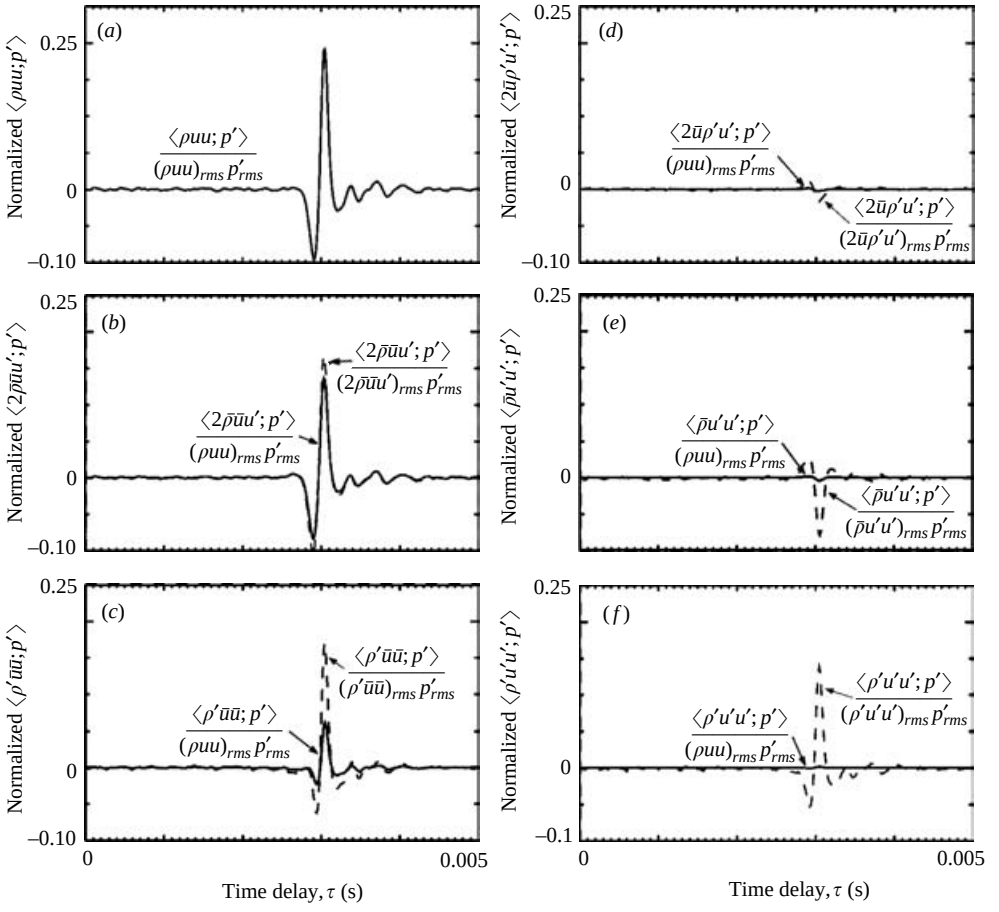

FIGURE 10. Normalized cross-correlation between sound pressure fluctuations and (*a*) ρuu fluctuations (*b*)–(*f*) various Reynolds decomposed terms of ρuu measured at $x/D = 10$ and centreline of $M = 1.4$ jet. The microphone was kept at $50D$ and 30° to the jet axis.

Data from the radial velocity v set-up is presented in figure 11 and table 3. Unlike ρuu, ρvv show significantly lower correlation with the far-field noise. The values are even lower when $\langle \rho vv; p' \rangle$ correlation are normalized by $(\rho uu)_{rms}$ as shown in table 3. That the $\langle \rho vv; p' \rangle$ correlation with 90° microphone is immeasurably small is of particular interest. The causality relation of equation (10) shows that $\langle \rho vv; p' \rangle$ correlation is the source for the 90° noise. Therefore, it had been expected that $\langle \rho vv; p' \rangle$ correlation from the 90° microphone would be significant. This was found to be incorrect. Note that the same time series of v and ρvv data when cross-correlated with a 30° microphone signal produced significant values above the noise floor. The v and ρvv fluctuations were measured from many axial and radial positions of different Mach-number jets, and nearly all correlation calculations with sound signal from a 90° microphone failed to show significant levels above the noise floor. The lack of correlation perhaps is explicable from the large-scale/fine-scale idea, which is discussed later. Correlation calculations performed between microphone signals and various Reynolds decomposed terms of ρvv showed another interesting result. The correlation from the third-order fluctuations $\langle \rho' v' v'; p' \rangle$ stood out as significantly larger than all other terms including that from the full term $\langle \rho vv; p' \rangle$. The prominence

Mach number	Probe x/D	Probe r/D	Microphone angle (deg.)	$\frac{\langle \rho uu; p' \rangle}{(\rho uu)_{rms} p'_{rms}}$	$\frac{\langle 2\bar{\rho}\bar{u}u'; p' \rangle}{(\rho uu)_{rms} p'_{rms}}$	$\frac{\langle 2\bar{\rho}\bar{u}u'; p' \rangle}{(2\bar{\rho}\bar{u}u')_{rms} p'_{rms}}$	$\frac{\langle \rho'\bar{u}\bar{u}; p' \rangle}{(\rho uu)_{rms} p'_{rms}}$	$\frac{\langle \rho'\bar{u}\bar{u}; p' \rangle}{(\rho'\bar{u}\bar{u})_{rms} p'_{rms}}$	$\frac{\langle 2\bar{u}\rho'u'; p' \rangle}{(\rho uu)_{rms} p'_{rms}}$
1.8	12	0	30	0.2207	0.1635	0.2094	0.0636	0.2129	−0.00214
1.8	6	0.45	30	0.0572	0.0406	0.0554	0.0201	0.0616	−0.0022
1.4	10	0	30	0.1919	0.1344	0.168	0.0624	0.17	−0.0021
0.95	10	0	30	0.0682	0.0592	0.064	0.01	0.028	0.0001
0.8	8	0	30	0.022	0.0198	0.019	0.0037	0.011	−0.0003

$\frac{\langle 2\bar{u}\rho'u'; p' \rangle}{(2\bar{u}\rho'u')_{rms} p'_{rms}}$	$\frac{\langle \bar{\rho}u'u'; p' \rangle}{(\rho uu)_{rms} p'_{rms}}$	$\frac{\langle \bar{\rho}u'u'; p' \rangle}{(\bar{\rho}u'u')_{rms} p'_{rms}}$	$\frac{\langle \rho'u'u'; p' \rangle}{(\rho uu)_{rms} p'_{rms}}$	$\frac{\langle \rho'u'u'; p' \rangle}{(\rho'u'u')_{rms} p'_{rms}}$
−0.042	−0.0025	−0.066	0.003	0.1707
−0.017	−0.0023	−0.028	0.0011	0.055
−0.0173	−0.0041	−0.0787	0.0014	0.14
0.001	−0.0019	−0.0095	0.0007	0.015
−0.0022	−0.0012	−0.0044	0.0003	0.0062

TABLE 2. Peak correlation coefficients between far-field sound pressure fluctuations and various Reynolds decomposed terms of ρuu.

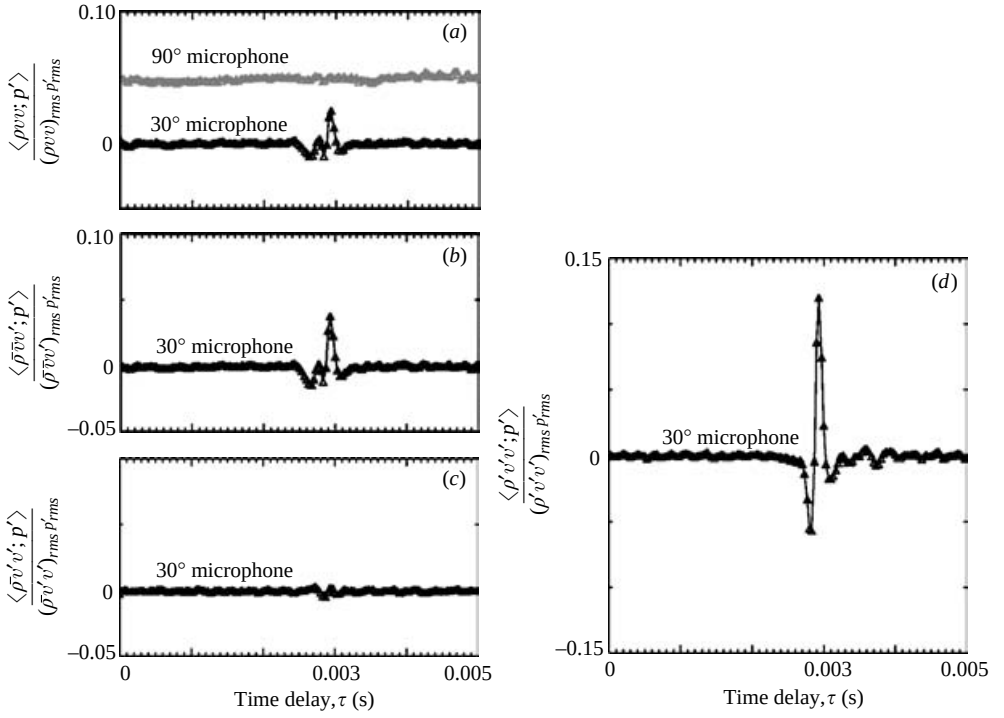

FIGURE 11. Normalized cross-correlation between sound pressure fluctuations and (*a*) ρvv fluctuations (*b*)–(*d*) various Reynolds decomposed terms of ρvv measured at $x/D = 10$ and centreline of $M = 1.4$ jet. The microphone was kept at $50D$ and the indicated polar angles.

of the third-order fluctuations as sound sources is consistent with the data from u velocity measurements.

At this point, a note on the uncertainty in the v-component measurement is worth mentioning. The present set-up produced high uncertainty in the time-averaged $\bar{v}$ measurement. Panda *et al.* (2004) showed that a $\pm 5\,\mathrm{m\,s^{-1}}$ uncertainty is expected from a set-up dedicated to the time-averaged measurements. The present dynamic measurement set-up produced even higher uncertainty in the time-averaged velocity estimates. This has led to significantly higher uncertainty in the calculation of ρvv than the $\rho' v' v'$ term.

Table 4 presents additional correlation data from turbulent density fluctuations $\langle \rho'; p' \rangle$. As can be seen, the correlation values are comparable and sometimes higher than that measured from other variables. This is especially true for the sound pressure fluctuations from 90° to the jet axis which correlates by an immeasurably small amount with most other flow parameters. It is a common practice in noise-source modelling to assume constant flow density. The present data, in contrast, show the utility of density fluctuation in tracing noise sources.

3.5. *Comparative study of correlation at various microphone angles*

Figure 12 shows variations in the maximum positive value of $\langle \rho uu; p' \rangle$ correlation, when the microphone polar angle is varied from 30° to 90° while the laser probe volume was kept fixed at the centreline and end of the potential core. The angles are measured from the downstream direction. The microphone radial distance from the nozzle was kept fixed at 50 diameters. Sound pressure fluctuations from the

Mach number	Probe x/D	Probe r/D	Microphone angle (deg.)	$\frac{\langle \rho vv; p' \rangle}{(\rho uu)_{rms} p'_{rms}}$	$\frac{\langle \rho vv; p' \rangle}{(\rho vv)_{rms} p'_{rms}}$	$\frac{\langle \bar{\rho}\bar{v}v'; p' \rangle}{(\bar{\rho}\bar{v}v')_{rms} p'_{rms}}$	$\frac{\langle \bar{\rho}v'v'; p' \rangle}{(\bar{\rho}v'v')_{rms} p'_{rms}}$	$\frac{\langle \rho'v'\bar{v}; p' \rangle}{(\rho'v'\bar{v})_{rms} p'_{rms}}$	$\frac{\langle \rho'v'v'; p' \rangle}{(\rho'v'v')_{rms} p'_{rms}}$
1.8	14	0	30	−0.00073	−0.0163	−0.0401	−0.0524	−0.0117	0.1596
1.8	14	0	90	0.00038	0.0088	0.0122	0.0088	Noise	−0.0231
1.8	6	0.48	30	−0.0027	−0.0369	−0.0456	−0.0153	−0.0095	−0.0525
1.8	6	0.48	90	Noise	Noise	Noise	Noise	Noise	Noise
1.4	10	0	30	0.0038	0.0245	0.0376	−0.0469	Noise	0.1201
1.4	10	0	90	Noise	Noise	Noise	Noise	Noise	−0.0128
0.95	10	0	30	−0.002	−0.0080	−0.0112	−0.0141	Noise	0.0283
0.95	10	0	90	Noise	Noise	Noise	Noise	Noise	Noise

TABLE 3. Peak correlation coefficients between far-field sound pressure fluctuations and various Reynolds decomposed terms of ρvv.

Mach number	Probe x/D	Probe r/D	Microphone angle (deg.)	$\dfrac{\langle \rho' ; p' \rangle}{\rho'_{rms} p'_{rms}}$
1.8	14	0	30	0.2414
1.8	14	0	90	−0.0336
1.8	6	0.48	30	−0.1039
1.8	6	0.48	90	−0.0081
1.4	10	0	30	0.17
1.4	10	0	90	−0.0266
0.95	10	0	30	−0.0368
0.95	10	0	90	Noise
0.8	8	0	30	0.0088

TABLE 4. Peak correlation coefficients between far-field sound pressure fluctuations and turbulent density fluctuations.

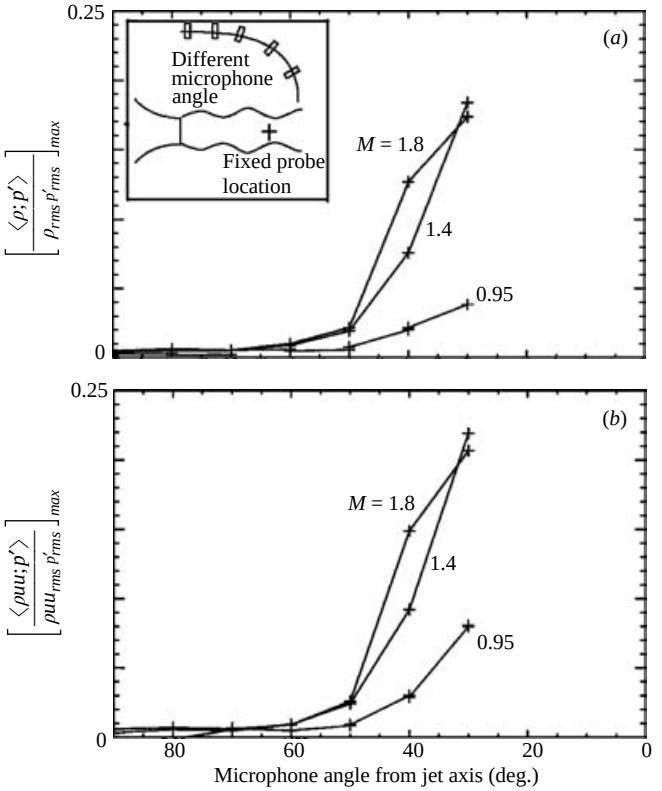

FIGURE 12. Angular dependence of peak correlation between microphone pressures and (*a*)ρ, (*b*) ρuu fluctuations. The laser probe was kept fixed at the centreline and $x/D = 8$ ($M = 0.95$ case), 10 ($M = 1.4$), or 12 ($M = 1.8$) while the microphone was moved at various angular locations on a $50D$ arc.

shallowest polar angle of 30° show the highest correlation. The correlations drop sharply to the noise floor at 60° and higher angles. A closer examination of $\langle \rho', p' \rangle$ and $\langle \rho uu, p' \rangle$ data from polar angles of 60° and higher for the supersonic plumes shows very weak correlation in the $0 \leqslant St \leqslant 0.4$ range. The coherence level (normalized cross-spectrum) is around 1 % or lower. One such coherence data set for the 90°

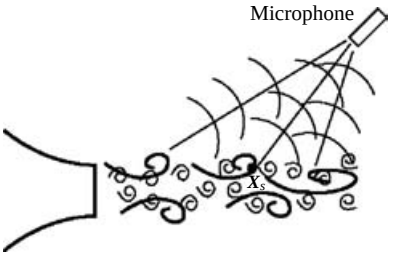

FIGURE 13. Schematic of large- and small-scale turbulent structures and noise radiation.

microphone location was presented earlier in Panda & Seasholtz (2002). Nevertheless, the present correlation study for the most part is identifying turbulent fluctuations that radiate close to the jet axis. The lack of correlation (or very weak values) at higher polar angles also implies existence of a second mechanism of noise generation which the present point measurement technique is unable to detect.

3.6. *Plausible reason for the directional variation of correlation coefficients*

Various aspects of the correlation data are better explained from a structural description of jet turbulence (Michalke 1977; Tam *et al.* 1996). The sound pressure fluctuations measured by a far-field microphone are due to the sum of the radiation from all turbulent eddies distributed in the entire jet plume. However, based on the extent of spatial coherence, the eddies can be broadly divided into large structures with coherence length scales of the order of a jet diameter, and fine structures of much smaller spatial coherence. Figure 13 provides a schematic description of the situation. It is believed that the present experiment picks up a contribution from the large structures and is unable to determine a contribution from fine-scale small eddies. Although the current technique measures correlation from a single point in the plume, the correlation values are extremely high for shallow angles. The radiation from various spatial locations of large structures is expected to be phase related; therefore, a single-point correlation reflects the contribution from the entire eddy. Theoretical calculations of Michalke (1977, 1983) show that the higher the spatial correlation of turbulence, the narrower the radiation angle. Additionally, frequency analysis of cross-correlation data demonstrates that the measured correlations are from low-Strouhal-frequency fluctuations. Once again this is a characteristic of large organized structures which radiates primarily in the downstream direction close to the jet axis (Morris & Tam 1979; Tam & Burton 1984). The quick drop in correlation with an increase of microphone polar angle, seen in figure 12, is reflective of inefficiency of the large-scale structures to radiate at higher angles. According to the model of Tam *et al.* (1996) fine-scale structures with little spatial coherence are primarily responsible for sound radiation at angles higher than 60°. Such eddies radiate more omni-directionally; the net sound field at a far-field point is a sum of the contributions from many such eddies with random phase relationships. Hence, correlation from a single measurement point in the plume is expected to be very small, below the experimental noise floor. This perhaps explains the inability of the present point-measurement scheme to identify noise sources for 90° radiation.

3.7. *Comparative study of correlation from various parts of jets*

For this part of the study, the microphone was kept fixed, at 50 diameters and 30° to the jet axis and the laser probe was moved from point to point in the plume.

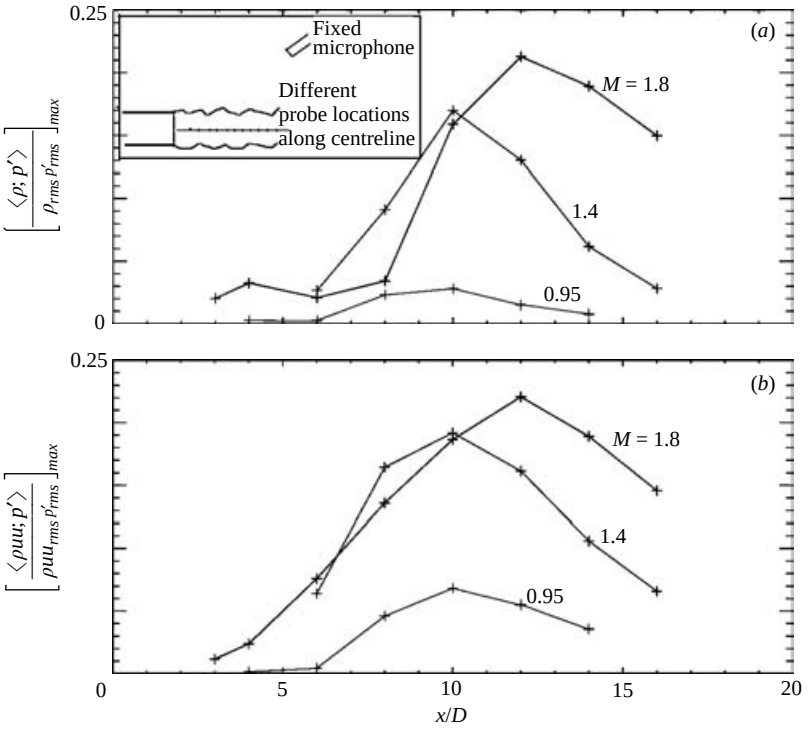

FIGURE 14. Axial dependence of peak correlation between microphone pressures and (*a*) ρ, (*b*) ρuu fluctuations measured along the centreline of the indicated Mach number plumes. The microphone was kept fixed at $50D$ and 30° to the jet axis.

Figure 14 shows the variation in peak correlation when the probe was moved along the centreline. The correlation values are small inside the potential core. Moving downstream, as the end of the core is approached, the correlations increase, with the highest values measured just downstream of the end of the potential core. The clasping of peripheral shear layer leading to merging and fragmentation of large turbulent eddies perhaps is the principle source of sound generation. Note that the potential core lengthens with Mach number owing to a decrease in shear-layer growth rate. The end appears around $x/D \approx 6$, 7 and 9 for Mach 0.95, 1.4 and 1.8 jets, respectively (Panda & Seasholtz 2002).

The variation of the correlation coefficient along the lip shear layer ($r/D = 0.45$) is very different from that along centreline. For figure 15, the microphone was again kept fixed at the same 30° location, while the probe volume was moved axially from point to point along $r/D = 0.45$. These data show a sharp difference between subsonic and supersonic plumes. In the subsonic Mach 0.95 plume, all correlations fall below the experimental noise floor, while in the supersonic Mach 1.4 and 1.8 cases significant correlation is measured. Note that the locations for the probe volume and the microphones were shifted by 90° azimuthally. This may also have contributed towards lower correlation from the shear layer. The difference between the centreline and the shear-layer behaviour prompted a study of radial dependence of the correlation coefficients. Figure 16 shows that indeed the highest correlation is measured from the centreline. The $\langle \rho uu; p' \rangle$ correlation progressively falls to the noise floor for $r/D > 0.6$. Note that these data once again support the prior conjecture of

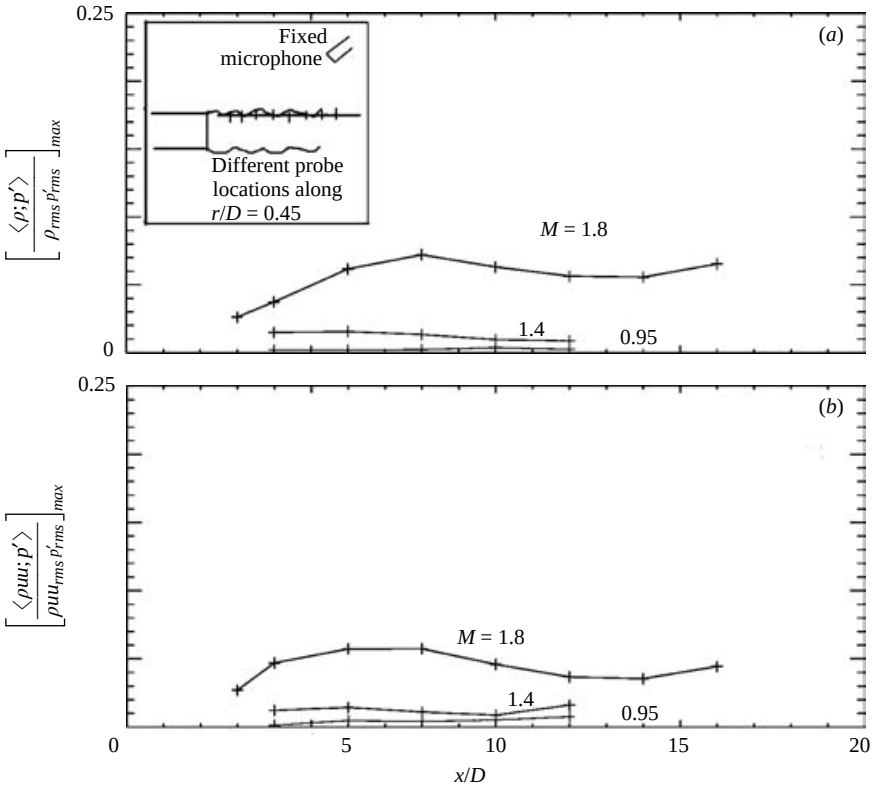

FIGURE 15. Axial dependence of peak correlation between sound pressure fluctuations and (*a*) ρ, (*b*) ρuu fluctuations measured along shear layer ($r/D = 0.45$) of the indicated Mach number plumes. The microphone was kept fixed at $50D$ and 30° to the jet axis.

large organized structures with radial coherence comparable to the jet diameter, being responsible for most of the measured correlation. Moreover, the radial dependence is reminiscent of radiation from axisymmetric mode of instability waves, which was attributed as the most efficient noise radiator by Michalke (1977) and Armstrong *et al.* (1977). Recall that figure 11 shows that the correlation from the radial velocity component $\langle v; p' \rangle$ is far weaker than that from the axial velocity component $\langle u; p' \rangle$, even for the shallow 30° microphone location. The axisymmetric mode has no radial velocity fluctuations at the centreline. Helical modes produce v fluctuations, yet they are poor radiators of sound. This may have contributed to the difference of the measured correlation from the two velocity components.

3.8. *Mach-number dependence of the correlation coefficients*

The maximum $\langle \rho uu; p' \rangle$ correlation measured from any position of the jet is found to be a strong function of the jet Mach number. Figure 17 presents a plot of the maximum correlation value measured with the sound pressure fluctuations from the 30° location. The laser probe was positioned beyond the end of the potential core and at the centreline for all Mach number conditions. The numerical values for the correlation coefficients are provided in table 2. Once again, it can be seen that the Mach wave emitting supersonic conditions produces the highest level, while the subsonic jets of $M \leqslant 0.8$ produce less than 2 % correlation. Panda & Seasholtz (2002) have presented schlieren photographs of the same jet as studied in the present

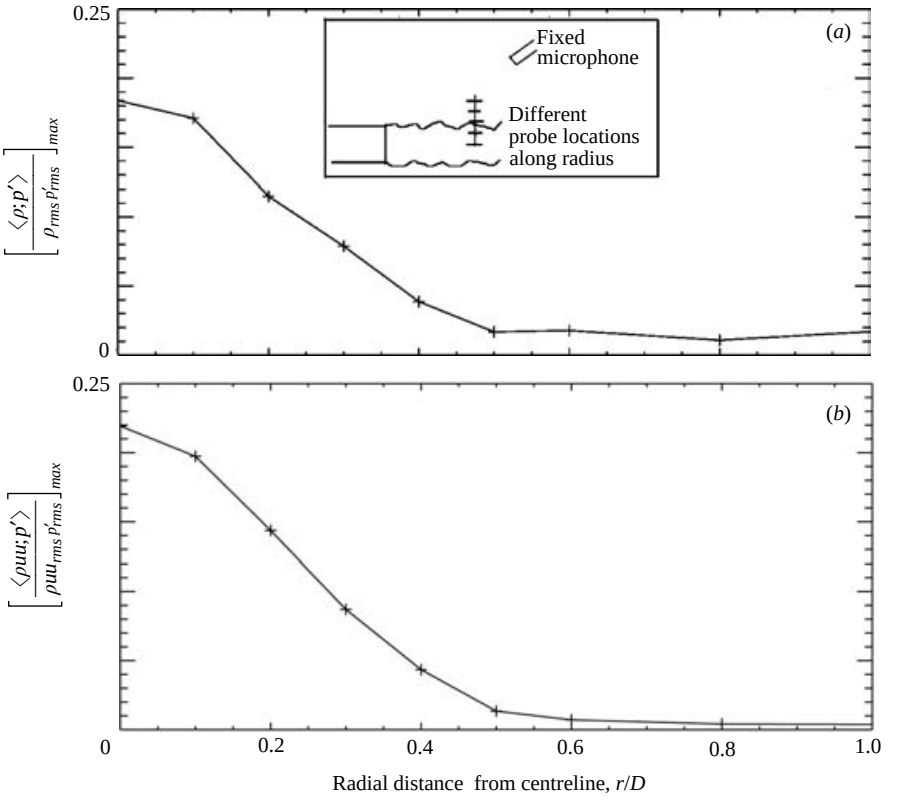

FIGURE 16. Radial dependence of peak correlation between sound pressure fluctuations and (*a*) ρ, (*b*) ρuu fluctuations, measured at $x/D = 10$ and various radial positions, in the Mach 1.4 plume. The microphone was kept fixed at $50D$ and 30° to the jet axis.

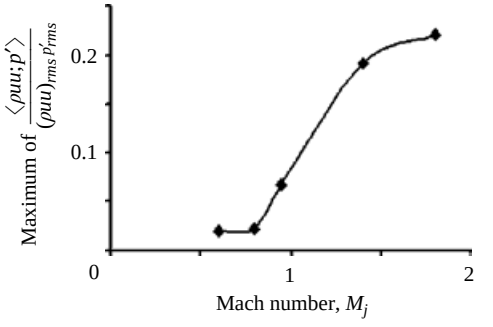

FIGURE 17. The Mach number dependence of the peak $\langle \rho uu; p' \rangle$ correlation measured with a fixed 30° microphone.

paper. These photographs demonstrate the presence of Mach wave emission (owing to the supersonic convective speed of some eddies) for the supersonic cases. The shock waves attached to the supersonically convected eddies makes an almost one to one connection between the near-field turbulence and the far-field sound pressure fluctuations. This is the reason for significantly higher correlation in supersonic plumes.

Finally, a comparison with correlation measurements from earlier work is in order. It is difficult to cross check the correlation values measured in the present experiment with many of the earlier experiments; since many earlier studies are on low-speed jets; also the issue of probe-intrusiveness has contaminated the result. However, some of the earlier experiments which employed non-intrusive laser-Doppler velocimetry show reasonable comparison. Schaffar (1979) used laser-Doppler velocimetry to measure u-fluctuations in unheated Mach 0.98 jet and cross-correlated with sound fluctuations measured by a microphone. The $\langle u'; p' \rangle$ correlation reported by Schaffar is comparable to the similar, Mach 0.95, data obtained in the present experiment. For example, Schaffar found $[\langle u'; p' \rangle / u_{rms} p_{rms}]_{max} = 0.055$, when the probe was positioned at $x = 10D$ and centreline and the microphone was located 30° to the axis. A nominally similar correlation number was obtained in the present $M = 0.95$ jet with identical probe and microphone locations (table 2). Schaffar (1979) also noticed that the correlation values fall nearly to zero for a microphone located at 45° to the jet axis. This is consistent with the observation made in figure 12. Additionally, an examination of correlation data from various radial positions presented in that paper shows similar lowering of correlation away from the centreline, as seen in figure 16. The difference in the relative positions of correlation maxima and minima in the self $\langle 2\bar{\rho}\bar{u}u'; p' \rangle$ and shear $\langle 2\bar{\rho}u'u'; p' \rangle$ components seen in figure 10 was also reported by Schaffar. This close comparison has provided further confidence in the measured data. Richarz (1980) used a laser-Doppler velocimetry to perform correlation measurements in an unheated low Mach 0.3 jet. The paper reports very weak correlations. Normalized cross-spectral density of the order of 0.005 was observed with a 40° microphone. Such low values are consistent with the trend shown in the Mach-number dependence plot of figure 17.

Almost all earlier studies were performed in subsonic jets, and therefore, the distinct difference between the subsonic and supersonic conditions was not observed. Additionally, some of the earlier experiments using intrusive probes show correlation from the peripheral shear layer at the early part of jet development. The two-microphone correlation technique of Armstrong *et al.* (1977) similarly attributed that in a subsonic Mach 0.5 jet the axial location of peak turbulence fluctuation of a given Strouhal number is also the location for peak correlation with noise at that frequency. This, however, is not supported by the present data except for the supersonic conditions where eddies attain supersonic speed relative to the ambient sound speed.

3.9. *Frequency analysis of cross-correlation data, cross-spectral density*

So far all correlation data were presented in the time domain. Figure 18 presents data in the frequency domain. The cross-spectral density value $S_{\rho uu,p'}$ is normalized by the time-averaged plume and ambient properties: a_0, U_j and ρ_0, as described in (13). Similar cross-spectral data between density and sound pressure fluctuations $S_{\rho,p'}$ is normalized as $S^*_{\rho,p'} = S_{\rho,p'}/(\rho_0 a_0)^2$. Note that figures 18(*b*)(i) and (*b*)(ii) were obtained from the same data set as used in the spectral plots of figure 8 and correlation plots of figures 9 and 10. The first point to be discussed is that figure 18 provides evidence to the claim that cross-correlation data are significantly free of the shot-noise effects. Unlike ρ and ρuu spectra in figure 8, the $S_{\rho,p'}$ and $S_{\rho uu,p'}$ cross-spectra rise two to three orders of magnitude above the noise floor. Moreover, the sharp peak at 430 Hz seen in ρuu spectra is absent in $S_{\rho uu,p'}$ cross-spectra. The second point to be made is that the turbulent fluctuations providing most of the correlations lie in the nominal

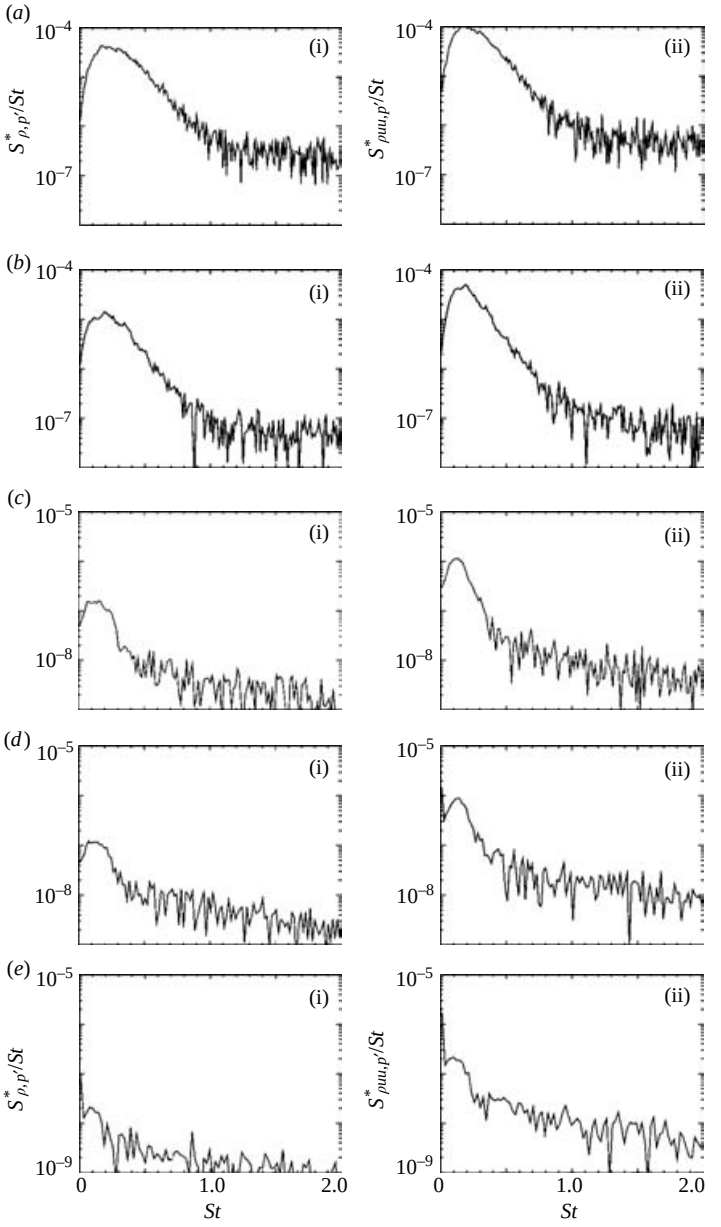

FIGURE 18. Normalized cross-spectrum of sound pressure fluctuations p' and (*a*)(i) to (*e*)(i) air density fluctuations, (*a*)(ii) to (*e*)(ii) ρuu fluctuations from the probe locations in various Mach number plumes. (*a*) $M = 1.8$, probe $x/D = 12$, centreline; (*b*) 1.4, 10, 0; (*c*) 0.95, 10, 0; (*d*) 0.8, 8, 0; (*e*) 0.6, 8, 0. The microphone was kept at 30° and 50*D*.

Strouhal number range $0 \leqslant St < 1.0$, with the peak value around $St = 0.2$. Once again it shows that the measured correlations are mostly due to the coherent structures; the contribution from small-scale fluctuations falls below the noise floor. Another noticeable trend is the similarity in the overall shapes of $S_{\rho,p'}$ and $S_{\rho uu,p'}$ cross-spectra over the entire Mach number range.

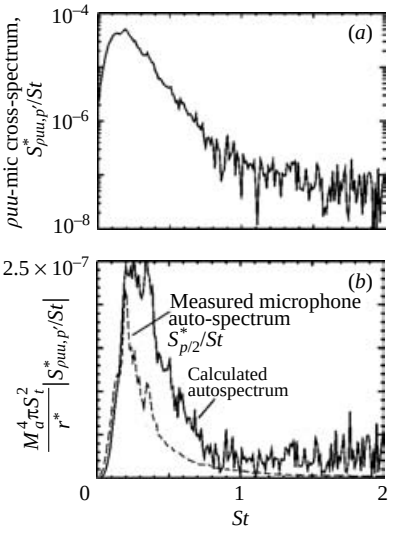

FIGURE 19. Relative contribution to the 30°-microphone auto-spectrum from ρuu-p' cross-spectra measured in the Mach 1.4 plume; probe location $x/D = 10$ and centreline. (*a*) ρuu-p' cross-spectra. (*b*) Calculated contribution from quadrupole term (equation (13)).

3.10. *Contribution to far-field noise from* $\langle \rho ; p' \rangle$ *and* $\langle \rho uu ; p' \rangle$ *correlation*

The causality principle, described in § 1, can be used to back-calculate far-field sound pressure fluctuations from the measured cross-correlations. This obviously is not a modelling approach, yet serves the purpose of estimating the fraction of noise generated from various regions of the jet. Figure 19 presents one such effort to calculate the auto-spectrum of sound pressure fluctuations at the 30° location (and $50D$ away from the nozzle exit) from a single-point cross-correlation measurement. The laser probe was placed at the centreline and downstream of the potential core where maximum correlation is measured. The probe and microphone locations are the same, for which correlation and spectral data are presented earlier. Figure 19(*b*) shows a comparison of the calculated auto-spectrum with the actual measured profile. Recall that the unevenness in the measured auto-spectra is an artefact of the reflection from large lenses placed close to the plume. The calculation procedures involve multiplication of cross-spectral density $S_{\rho uu,p'}$, by various terms, most importantly by frequency squared, as described in (13). The dashed curve represents the left-hand sides of the equations and the solid curve the right-hand side. Note that the causality equations require an integration of all cross-spectra measured over the entire jet plume. This has not been attempted in the present work. Instead, the calculated auto-spectrum should be interpreted as the effectiveness of a unit volume of flow, centred at the laser probe, in creating sound pressure fluctuations at the microphone location. Figure 19(*b*) shows that the measured correlations are so high that a unit volume produces more noise than the measured auto-spectrum. Perhaps the only way that a final lower value of the microphone auto-spectrum can be reconciled is by assuming phase cancellations from different regions of the jet.

4. Summary and conclusions

A recent advancement in the molecular Rayleigh-scattering technique, to simultaneously measure velocity and density fluctuations in high-speed flows, has

been used to identify sound sources in supersonic and high subsonic unheated free jets. The particle-free non-invasive technique involves passing a narrow CW laser beam through a jet plume and collecting molecular scattered light from a small region on the beam. A part of the collected light is directly measured to detect scattering intensity, which is proportional to air density. The rest of the collected light was passed through a Fabry–Perot interferometer to measure the Doppler shift associated with one component of jet velocity. The Fabry–Perot was operated in an imaging mode and the fringe formed at the image plane was split into two parts. The ratio of light intensity is related to velocity.

Two separate arrangements of collection optics were used to measure either ρ, u or ρ, v simultaneously. Time histories measured from various points in the plume were Fourier transformed to obtain spectra. A comparison shows that the ρ and u spectra are similar in shape while the v spectrum is different, especially in the centreline of the jet. The $\rho - u$ cross-spectra show progressively decreasing correlation with increasing frequency. The spectral data suffer from a large bias error due to electronic shot noise; yet the correlation data between the turbulent fluctuations and far-field sound pressure fluctuations are relatively error-free.

The noise emitted by the jets was measured by microphones placed in the far field and at polar angles from 30° to 90° to the downstream direction. The microphone signals $p'(t)$ were correlated separately with $\rho(t), u(t), v(t), \rho uu(t)$ and $\rho vv(t)$ signals measured from various points in the flow. The non-intrusiveness of the laser-based technique avoids the probe-interference effects that have plagued previous attempts at source identification via causality method. Some significant observations from this study are the following:

(*a*) Out of all flow parameters, the ρuu fluctuations are found to provide the highest correlation with the far-field noise. This is closely followed by axial velocity u and density ρ fluctuations. Indeed, $\langle \rho uu; p' \rangle$ and $\langle \rho; p' \rangle$ correlations are strikingly similar in all respects: absolute magnitudes of normalized correlations, frequency distribution, and dependence on the microphone and probe volume locations. The v and ρvv fluctuations are found to be poorly correlated with p'.

(*b*) Frequency dependence of the cross-spectral data and variation of the correlation coefficients with microphone polar angles showed that the large coherent structures contributed most to the correlation coefficients. Cross-spectral analysis of ρuu and p' fluctuations shows that the turbulent fluctuations in the frequency range $0 \leqslant St < 1$ were providing most of the measured correlation. This Strouhal frequency range is typical of large organized structures. A study of the variation of correlation coefficients with microphone polar angle show that the sound pressure fluctuations closest to the jet axis (30°) provide the highest correlation; the magnitude falls sharply until 60°, beyond which data were mostly below the experimental noise floor. This observation is consistent with previous analysis (for example, Michalke 1977) that has shown that the larger the spatial coherence of turbulence, the narrower the radiation angle.

(*c*) The spatial dependence of the correlation coefficients was studied by moving the laser probe volume from point to point in the flow while keeping the microphone fixed. The strongest sound-producing region was found to lie along the centreline and beyond the end of the potential core. For example, in the Mach 1.4 jet, the highest correlation was measured from $x/D = 10$ on the centreline (the potential core ended at $x/D \approx 7$). When the laser probe was moved radially, the $\langle \rho vv; p' \rangle$ correlation was found to decrease monotonically and fall below the noise floor beyond the edge of the turbulent flow. Correlation from the lip shear layer is found to be Mach-number dependent. Significant correlations were measured all along the lip shear layer of

supersonic plumes, while the subsonic plumes did not show any such correlation. These observations are consistent with our earlier work (Panda & Seasholtz 2002) where differences between subsonic and supersonic jets were attributed to the inception of the 'Mach wave' emission process. 'Mach waves' are emitted when some eddies attain convective velocity higher than ambient. Far-field propagation of the shock waves attached to eddies produce the high correlation in supersonic jets.

(*d*) To help various jet-noise modelling efforts, Reynolds decomposition was performed on the full ρuu term, and the individual fluctuating terms were separately correlated with the far-field noise. It was found that correlations from the first-order fluctuations, $\langle 2\bar{\rho}\bar{u}u'; p'\rangle$ and $\langle \rho'\bar{u}\bar{u}; p'\rangle$, provided the largest contribution towards the full correlation $\langle \rho uu; p'\rangle$. This was closely followed and sometimes superseded by the third-order terms $\langle \rho', u'u'; p'\rangle$. Contributions from terms second order in fluctuations were the weakest of all.

We acknowledge help from Amy F. Mielke of NASA Glenn Research Center with data acquisition during a part of the experiment. J. P. is grateful to Professor Philip J. Morris of Pennsylvania State University and Dr Abbas Khavaran of QSS at NASA Glenn Research Center for insightful discussions and suggestions on data analysis.

REFERENCES

Armstrong, R. R., Michalke, A. & Fuchs, H. V. 1977 Coherent structures in jet turbulence and noise. *AIAA J.* **15**, 1011–1017.

Colonius, T., Lele, S. K. & Moin, P. 1997 Sound generation in a mixing layer. *J. Fluid Mech.* **330**, 375–409.

Elliott, G. S. & Samimy, M. 1996 Rayleigh scattering technique for simultaneous measurements of velocity and thermodynamic properties. *AIAA J.* **34**, 2346–2352.

Fedorchenko, A. T. 2000 On some fundamental flaws in present aeroacoustic theory. *J. Sound Vib.* **232**, 719–782.

Ffowcs Williams, J. E. 1973 Technical evaluation report. *AGARD CP 131 on Noise Mechanisms*, VII–XIX.

Forkey, J. N., Lempert, W. R. & Miles, R. B. 1998 Accuracy limits for planer measurements of flow field velocity, temperature and pressure using filtered Rayleigh scattering. *Exps. Fluids* **24**, 151–162.

Goldstein, M. E. 1976 *Aeroacoustics*. McGraw–Hill.

Hurdle, P. M., Meecham, W. C. & Hodder, K. 1974 Investigation of the aerodynamic noise generation region of a jet engine by means of the simple source fluid dilatation model. *J. Acoust. Soc. Am.* **56**, 1708–1721.

Hussain, A. K. M. F. & Zaman, K. B. M. Q. 1981 The 'preferred mode' of the axisymmetric jet. *J. Fluid Mech.* **110**, 39–71.

Khavaran, A., Krejsa, E. A. & Kim, C. M. 1992 Computation of supersonic jet mixing noise for an axisymmetric CD nozzle using k-ε turbulence model. *30th AIAA Aerospace Sciences Meeting, Reno. AIAA Paper* 92-0500.

Lee, H. K. & Ribner, H. S. 1972 Direct correlation of noise and flow of a jet. *J. Acoust. Soc. Am.* **52**, 1280–1290.

Lighthill, M. J. 1954 On sound generated aerodynamically I. General theory. *Proc. R. Soc.* A **221**, 564–587.

Lilley, G. M. 1974 On the noise from jets. *AGARD CP*-131, 13.1–13.12.

Michalke, A. 1977 On the effect of spatial source coherence on the radiation of jet noise. *J. Sound Vib.* **55**, 377–394.

Michalke, A. 1983 Some remarks on source coherence affecting jet noise. *J. Sound Vib.* **87**, 1–17.

Miles, R. B., Lempert, W. R. & Forkey, J. N. 2001 Laser Rayleigh scattering. *Meas. Sci. Technol.* **12**, R33–R51.

Morris, P. J., Boluriaan, S., Lilley, G. M. & Long, L. N. 2002 Two-point cross correlations of turbulence and noise predictions: analysis and simulation. *AIAA Paper* 2002-0071.

Morris, P. J. & Tam, C. K. W. 1979 On the radiation of sound by the instability waves of a compressible axisymmetric jet. In *Mechanisms of Sound Generation in Flows* (ed. E. A. Muller). Springer.

Panda, J. & Seasholtz, R. G. 2002 Experimental investigation of density fluctuations in high-speed jets and correlation with generated noise. *J. Fluid Mech.* **450**, 97–130.

Panda, J., Seasholtz, R. G., Elam, K. A. & Mielke, A. F. 2004 Time-averaged Velocity, Temperature and Density Surveys of Supersonic Free Jets. *2004 ASME Heat Transfer/ Fluids Engineering Summer Conference. ASME Paper HT-FED* 2004-56856.

Proudman, I. 1952 The generation of noise by isotropic turbulence. *Proc. R. Soc.* A **214**, 119–132.

Rackl, R. 1973 Two causality correlation techniques applied to jet noise. PhD thesis, University of British Columbia.

Richarz, W. G. 1980 Direct correlation of noise and flow of a jet using laser Doppler. *AIAA J.* **18**, 759–765.

Saleh, B. E. A. & Teich, M. C. 1991 *Fundamentals of Photonics*. John Wiley.

Schaffar, M. 1979 Direct measurements of the correlation between axial in-jet velocity fluctuations and far field noise near the axis of a cold jet. *J. Sound Vib.* **64**, 73–83.

Seasholtz, R. G. & Panda, J. 2000 Rayleigh scattering diagnostic for simultaneous measurements of dynamic density and velocity. *AIAA Paper* 2000-0642.

Seasholtz, R. G. & Panda, J. 1999*a* Rayleigh scattering diagnostic for dynamic measurement of velocity and temperature. *AIAA Paper* 99-0641.

Seasholtz, R. G., Panda, J. & Elam, K. A. 2001 Rayleigh scattering diagnostics for dynamic measurement of velocity fluctuations in high speed jets. *AIAA Paper* 2001-0847.

Seasholtz, R. G., Panda, J. & Elam, K. A. 2002 Rayleigh scattering diagnostic for measurement of velocity and density fluctuation spectra. *40th AIAA Aerospace Sciences Meeting. AIAA Paper* 2002-0827.

Seiner, J. M. 1974 The distribution of jet source strength intensity by means of a direct correlation technique. PhD dissertation, The Pennsylvania State University, Department of Aerospace Engineering.

Seiner, J. M. & Reethof, G. 1974 On the distribution of source coherency in subsonic jets. *AIAA Paper* 74-4.

Siddon, T. E. 1973 Noise source diagnostics using causality correlations. *AGARD CP* 131, *Noise Mechanisms*, 7-1–7-13.

Tam, C. K. W. 1998 Jet noise: since 1952. *Theoret. Comput. Fluid Dyn.* **10,** 393–405.

Tam, C. K. W. 2001 On the failure of the acoustics analogy theory to identify the correct noise sources. *AIAA Paper* 2001-2117.

Tam, C. K. W. & Burton, D. E. 1984 Sound generated by instability waves of supersonic flows. Part 2. Axisymmetric jets. *J. Fluid Mech.* **138**, 249–271.

Tam, C. K. W., Golebiowski, M. & Seiner, J. M. 1996 On the two components of turbulent mixing noise from supersonic jets. *AIAA Paper* 96-1716.

Tam, C. K. W. & Zaman, K. B. M. Q. 2000 Subsonic jet noise from nonaxisymmetric and tabbed nozzles. *AIAA J.* **38**, 592–599.

Welch, P. D. 1967 The use of fast Fourier transform for the estimation of power spectra: a method based on time averaging over short, modified periodograms. *IEEE Trans. on Audio and Electroacoustics*, **AU-15**, 70–73.